~~Bulk~~ Ensemble mean density and its connection to other microphysical properties of falling snow as observed in Southern Finland

Jussi Tiira[1], Dmitri N. Moisseev[1, 2], Annakaisa von Lerber[2, 3], Davide Ori[1, 4], Ali Tokay[5, 6], Larry F. Bliven[7], and Walter Petersen[8]

[1]Department of Physics, University of Helsinki, Helsinki, Finland
[2]Finnish Meteorological Institute, Helsinki, Finland
[3]School of Electrical Engineering, Aalto University, Finland
[4]Department of Biological Geological and Environmental Sciences and Department of Physics and Astronomy, University of Bologna, Bologna, Italy
[5]Joint Center for Earth Systems Technology, University of Maryland, Baltimore County, Baltimore
[6]NASA Goddard Space Flight Center, Greenbelt, MD
[7]NASA GSFC/Wallops Flight Facility, Wallops Island, VA
[8]NASA-MSFC Earth Science Office, National Space Science and Technology Center, Huntsville, AL

Correspondence to: Jussi Tiira (jussi.tiira@helsinki.fi)

Abstract. In this study measurements collected during winters 2013/2014 and 2014/2015 at the University of Helsinki measurement station in Hyytiälä are used to investigate connections between ~~snow bulk~~ ensemble mean snow density, particle fall velocity and parameters of the particle size distribution (PSD). The ~~bulk~~ density of snow is derived from measurements of particle fall velocity and PSD, provided by a particle video imager, and weighing gauge measurements of precipitation rate. Validity of the retrieved density values is checked against snow depth measurements. A relation retrieved for ~~bulk~~ the ensemble mean snow density and median volume diameter is in general agreement with previous studies, but observed to vary significantly from one winter to the other. From these observations, characteristic mass-dimensional relations of snow are retrieved. For snow rates more than 0.2 mm h^{-1}, a correlation between the intercept parameter of normalized gamma PSD and median volume diameter was observed.

1 Introduction

Due to a variety of ice particle types and shapes, representation of winter precipitation in models (Woods et al., 2007; Morrison and Milbrandt, 2015) and in ground, airborne, and satellite remote sensing retrievals (Sekhon and Srivastava, 1970; Matrosov, 1997; Wood et al., 2013) is a topic of continuous interest. Both models and retrieval algorithms rely on a prior knowledge of snowflake mass (or density), shape and fall velocity, which are typically expressed as functions of a characteristic particle size (Pruppacher and Klett, 1996). Furthermore, information on possible particle size distributions ~~(PSDs)~~ is also required. Even though some of the microphysical properties of ice particles are not independent, e.g. fall velocity can be computed

from particle mass and shape (Böhm, 1989; Khvorostyanov and Curry, 2005; Mitchell and Heymsfield, 2005; Heymsfield and Westbrook, 2010), the remaining degrees of freedom are rather numerous.

Historically, measurements of snowflake properties have been carried out on particle-by-particle basis (e.g., Magono and Nakamura, 1965; Locatelli and Hobbs, 1974; Mitchell, 1996). While we may still regard such measurements as the more precise and detailed, due to the sheer amount of time needed for such experiments and corresponding data analysis, these studies are limited to a relatively small number of observed ice particles. After introduction of robust optical instruments capable of measuring particle size, shape and in some cases fall velocity, e.g. 2D-video disdrometer (2DVD, Hanesch, 1999; Schönhuber et al., 2007), particle size velocity (Parsivel) laser-optical disdrometer (Löffler-Mang and Joss, 2000; Löffler-Mang and Blahak, 2001), hydrometeor velocity size detector (HSVD, Barthazy et al., 2004), snow video imager (SVI, Newman et al., 2009) and multi-angle snowflake camera ~~(MASC, Garrett and Yuter, 2014)~~ (MASC, Garrett et al., 2012) , continuous recording of ice particle properties became possible. It should be noted, in comparison to surface based observations, aircraft measurements have a much longer history in determining ice particle microphysical properties, and were carried out in different types of clouds and climate regimes (Pruppacher and Klett, 1996). A typical limitation of automatic observations of ice particle properties, however, is that only a subset of needed parameters is directly measured.

By combining optical disdrometer observations with other measurements, ~~i.e.~~e.g. by radar or precipitation gauge, physical properties such as mean snow density can be derived. Huang et al. (2010) have used a C-band weather radar observations of equivalent reflectivity factor, Z_e, in combination with a 2DVD to derive snow density-dimensional relation and to infer more consistent Z_e–snowfall rate, SR, relations. Another method for snow density retrieval is based on solving aerodynamic equations to derive particle mass from observed fall velocity and particle effective projected area as proposed by Böhm (1989) and applied by Hanesch (1999) and more recently by Szyrmer and Zawadzki (2010) and Huang et al. (2015) . Brandes et al. (2007), hereafter referred to as B07, used a combination of a weighing gauge and a 2DVD to derive mean bulk density-median volume diameter relations and to document relations between PSD parameters for Colorado winter storms. Their approach is similar to the one used by Heymsfield et al. (2004) who have combined aircraft PSD and ice water content observations to derive ~~bulk~~ mean snow density and average mass-dimensional relations for ice particles. Albeit using slightly different definitions, both B07 and Heymsfield et al. (2004) derive effective ice densities for ~~ice particle populations~~ensembles of ice particles, but there is a difference in terminology. ~~We follow terminology of B07 and~~ Heymsfield et al. (2004) and many others have used the term (particle) bulk density to refer to the ~~derived densities as bulk densities whereas Heymsfield et al. (2004) talk about effective densities of particle populations. Another method for snow densityretrieval is based on solving aerodynamic equations to derive particle mass from observed fall velocity and particle effective projected area as proposed by Böhm (1989) and applied by Hanesch (1999) and more recently by Szyrmer and Zawadzki (2010) and Huang et al. (2015)~~ density of individual ice or snow particles defined as the ratio of mass of a particle having a size D to its assumed volume: $\rho = \rho(D)$. In most of such cases, the word "bulk" is used to emphasize the inclusion of hollows within particles. The term "(mean) bulk density" is sometimes used also when referring to the mean density of an ensemble of particles representing the whole PSD, i.e. $\bar{\rho} = \bar{\rho}(D_0)$ (e.g., B07) , whereas Heymsfield et al. (2004) used the term population-mean effective density. In this study we

derive the volume flux weighted snow density, similar to e.g. B07 , and refer to it as ensemble mean density, $\bar{\rho}$, to avoid possible confusion.

This paper documents connection between ~~bulk~~ ensemble mean density and other microphysical properties of snow as observed in Southern Finland. ~~From the estimated bulk density~~Using the estimated $\bar{\rho}$, average mass-dimensional relations characteristic to studied snowfall events are defined. In order to derive ~~bulk snow~~ ensemble mean density, a method proposed by B07 was used. However, instead of a 2DVD, a new generation of the SVI is employed. It is shown that, despite simpler construction compared to the 2DVD, this instrument's data is suitable for such studies.

Even though this study is based on retrieval of ensemble mean snow density and not mass-dimensional relations directly, which could be more easily applied to radar retrievals and numerical weather prediction (NWP). There are a number of applications of such relations. Aikins et al. (2016) used $\bar{\rho}(D_0)$ to convert particle size distribution observations to precipitation rate. Tong and Xue (2008); Dolan and Rutledge (2009); Matrosov et al. (2009); Huang et al. (2010); Zhang et al. (2011) used mean snow density-median volume diameter relations for characterizing winter precipitation microphysics by radar. Kneifel et al. (2015) showed a connection between mean snow density and multi-frequency radar observations. Thompson et al. (2008) used the density relation by B07 , and Iguchi et al. (2012) applied a similar density retrieval method to improve parametrization of snow microphyics in NWP models, for example.

2 Measurements

2.1 Measurement setup

Measurements were made at the University of Helsinki Hyytiälä Forestry Field Station, Finland (N61°50′37″, E24°17′16″) during the Biogenic Aerosols Effects on clouds and Climate (BAECC) field campaign (Petäjä et al., 2016) and during the consecutive winter of 2014/15. BAECC was a joint experiment between the University of Helsinki, the Finnish Meteorological Institute and the United States Department of Energy Atmospheric Radiation Measurement (ARM) program. From 1 February through 12 September 2014 the second ARM Mobile Facility (AMF2) was deployed to the measurement site. The measurement setup was designed for snowfall intensive observation period (IOP) of BAECC, called BAECC Snowfall Experiment (SNEX), which was undertaken from 1 February though 30 April 2014 and focused on measurements of snow microphysics. However, in order to extend the dataset, the measurements were continued upon completion of BAECC. In total, 23 snowfall cases from winters 2013/14 and 2014/15 ~~, where a number of events extended over a couple of days,~~ were used in this study as summarized in Table 1. The snowfall cases were selected based on measurements of liquid water equivalent (LWE) precipitation accumulation by a weighing gauge, snow depth using a laser sensor, and temperature measured by the automatic weather station of FMI located 500 m distance from the measurement site. Only precipitation cases, where temperature was below or equal to 0°C were chosen, and when occasionally the temperature during the event rose above 0°C, the data was omitted.

The experiments in both winters were organized in collaboration with the National Aeronautics and Space Administration (NASA) Global Precipitation Measurement (GPM) Mission ground validation (GV) program. The surface precipitation measurements are carried out using a number of collocated instruments, such as NASA Particle Imaging Package (PIP), two

OTT Pluvio^2 weighing gauges, two Parsivel^2 laser disdrometers (Tokay et al., 2014), a 2DVD and a laser snow depth sensor by Jenoptik. To minimize effects of wind, a Double-Fence Intercomparison Reference (DFIR) wind protection (Rasmussen et al., 2012) was build on site as shown in Fig. 1 and discussed in more detail in Petäjä et al. (2016). Inside of the DFIR, the 2DVD, one of the OTT Pluvio^{2}s and one of the Parsivel^2 disdrometers were placed. In addition to the precipitation sensors, 3D-anemometers were deployed. The wind measurements were carried out at the heights of precipitation instrument sampling volumes. In this study data from the NASA PIP disdrometer and both OTT Pluvio^2 gauges are used.

2.2 Particle Imaging Package (PIP)

The NASA Particle Imaging Package is the new generation of the SVI. The PIP, like the SVI, consists of a halogen lamp and a charge-coupled device (CCD) full frame camera with sensor resolution of 640×480 pixels. The main differences between PIP and SVI are the camera and improved software. The camera is now capable of imaging with a frame rate of 380 frames per second, enabling measurements of particle fall velocities. The distance between the lamp and the camera lens is approximately 2 m. The lens focus is set at 1.3 m, where the field of view (FOV) is 64×48 mm, and the image resolution thereby 0.1×0.1 mm. The main advantage of PIP, as well of SVI, over other disdrometers is the open particle catch volume, which minimizes effect of wind on quantitative precipitation measurements (Newman et al., 2009).

The instrument records shadows of particles as they fall through the observation volume. Given the camera frame rate, multiple images of a particle are recorded and used to estimate its fall velocity. The depth of field (DOF) is determined by the processing software either rejecting or not detecting particles that are out of focus. Thus, the observation volume is defined by the FOV and the DOF. The expected particle size error due to the blurring effect is 18 ~~%~~ % (Newman et al., 2009). From the recorded particle images a number of parameters describing particle geometrical properties are calculated with National Instruments IMAQ - software. The measured diameter is given as the equivalent disk diameter, which is the diameter of a disk with the same area as the area of a particle image. Other parameters, such as particle orientation, ~~equivalent ellipse major and minor axes~~ and bounding box width and height are also recorded. The aspect ratio of a particle is derived by fitting an ellipse to the bounding box utilizing the orientation of the particle. The aspect ratio is the minor axis in respect to major maxis of the fitted ellipse. The major axis also defines the minimum circumscribing disk, and the area ratio is defined as total area of shadowed pixels in respect to area of the circumscribing disk.

2.3 Weighing gauges and anemometers

The measurement setup includes two OTT Pluvio^2 weighing gauges~~. The one inside of the DFIRhas an orifice~~ , one inside and one outside the DFIR, with orifices of 200 cm^2 and ~~the one outside an~~ 400 cm^2~~orifice~~, respectively. There are differences in wind shielding as well. The Pluvio^2 200 is equipped with a Tretyakov wind shield and the Pluvio^2 400 with a combination of Tretyakov and Alter wind shields, as seen in the forefront in Fig. 1.

The gauges output several products of precipitation rate and accumulation. In this study, a non-real-time accumulation product is used as it is filtered for various sources of errors such as changes in the bucket mass due to evaporation, and as such should yield the most precise precipitation rate estimate among the output products. Because of the filtering, there is a 5 min

delay in the recorded time series, which needs to be taken into account when comparing to other instruments. The precipitation accumulation values are recorded with a resolution of 0.001 mm, but non-real-time accumulation is output with a resolution of 0.05 mm.

The 3D - anemometer manufactured by Gill is located approximately at the height of the PIP on the field, respectively. The wind parameters, horizontal and vertical speed and horizontal direction, of Gill anemometer are measured every 10 s and averaged over 60 s. The mean and maximum of the 60 second wind speed averages and the mean wind direction for each event are given in the Table 1.

2.4 Snow depth sensor

The laser snow depth sensor, Jenoptik SHM30, is located on the measurement field, next to Pluvio^2 400. It is an ~~optic~~ optical sensor, which measures the snow depth by comparing signal phase information of the modulated visible laser light. It is a point measurement, hence the piling of wind driven snow or random branches and leaves drifting on the snow pack can cause misreadings. To reduce this we have sheltered the measurement spot with a small wind fence and the instrument structure excluding the measurement pole is buried under the ground to prevent the piling of snow. The data is recorded every minute.

3 Retrievals of ~~bulk~~ ensemble mean density, velocity-dimensional relations and PSD

Observations from the PIP and one of the weighing gauges are combined to retrieve ~~bulk snow~~ snow ensemble mean density. Typically the gauge located inside of the DFIR, the Pluvio^2 200, is used for this retrieval. On a couple of days this gauge was not operational and data from the Pluvio^2 400 ~~outside~~ located outside of the DFIR was used instead. These dates are marked in Table 1 with asterisks in the LWE precipitation rate column. As seen in the Table 1 the differences in accumulated LWE recorded by the two Pluvio^{2}s are small, largest being 15 %. Pluvio^2 200 inside the DFIR is typically measuring higher accumulations, which is expected because of the ~~smaller orifice, but there is no~~ better wind protection. However, the observations do not show a clear indication that ~~this would be depended on~~ the observed precipitaiton accumulation difference depends on the wind speed. However, the difference seems to increase in respect to certain wind directions. There are two openings from the measurement field, one to a road crossing (approx. 130°) and the other to small field (approx. 180°). If the wind is blowing from these directions the difference between the two gauges seem to increase.

The retrieval procedure is described below and is similar to the one presented by B07, but with notable modifications. Prior to retrieval of ~~snow bulk density~~ $\bar{\rho}$, PSD and velocity-dimensional relations are estimated. It was found, however, that the density retrieval is highly sensitive to the integration time. To minimize this, a variable integration time determined by the precipitation accumulation is used. The same integration time was applied to compute PSD parameters and v-D relations.

3.1 Particle size distribution~~(PSD)~~

The PSDs are calculated from the PIP records of particles that fell through the observation volume. The observed distributions are defined with respect to equivalent area diameter D_{PIP}, which is different from the apparent diameter of the 2DVD

and maximum particle dimensions used in other studies (e.g., Heymsfield et al., 2004). Wood et al. (2013) studied differences between diameter definitions and found that the diameter recorded by SVI is approximately 0.82 of maximum particle dimension. We performed a similar study by examining mean dimensions of ~~a rotated spheroid~~ rotated ellipsoids on a single projection, as shown in Fig. 2. The ellipsoids were defined by a long dimension a and a short dimension b lying nominally in the horizontal plane along the x and ~~found that the PIP diameter is roughly equal to 0.92 of a~~ y-axes, respectively, and a short vertical dimension c lying nominally along the z-axis. The particle orientation was defined by Gaussian distribution of canting angles with a standard deviation of 9° (Matrosov et al., 2005a) and a uniform distribution of azimuth angles. The equivalent area diameters D_{PIP} of simulated particles were estimated as their projected areas onto the x-z plane and the resulting values were averaged over all orientations. The ratios of mean D_{PIP} to the particle volume equivalent diameter, i.e. the diameter for which the particle volume $V(D) = \frac{\pi}{6} D^3$~~. This conversion factor is the mean value for spheroidal particles with axis ratio~~ , for a number of combinations of vertical and horizontal aspect ratios are shown in Fig. 2. Assuming spheroids (Matrosov, 2007) and taking the typical vertical aspect ratio $c/a = 0.6$ (Korolev and Isaac, 2003; Matrosov et al., 2005b) we found that D_{PIP} is roughly equal to 0.92 of a volume equivalent diameter. As can be seen, the conversion factor varies between 0.8 and 1. For ice particles with axis ratios smaller than 0.4, i.e. pristine ice crystals, this factor could approach 1.4. From this analysis we can conclude that the largest expected error is associated with observations of ice crystals. Dimensions of snowflake aggregates and graupel like particles are expected to be captured with a smaller error. In this study the same conversion factor of ~~0.6 (Korolev and Isaac, 2003; ?)~~ , 0.92 is used for all the cases. As can be seen in Fig. 3 the median area and aspect ratios of the particles are 0.65 and ~~orientation defined by Gaussian distribution of canting angles with the standard deviation of 9° (?) and uniform distribution of azimuth angles. The conversion factor is used in our study and all the results are presented~~ 0.72, respectively. These observations also support our choice of a mean particle shape and the corresponding diameter transformation. Therefore, the results presented in the rest of the manuscript are using this volume equivalent diameter proxy.

Prior to calculations of PSD parameters, recorded PSD data is filtered to remove spurious observations of large particles. Following the procedure described in ~~(Leinonen et al., 2012)~~ **?** , records of large particles were ignored if there was a gap of more than three consecutive PSD diameter bins. The bin size was set to 0.25 mm during the BAECC experiment and it was reduced to 0.2 mm for the winter 2014/2015. The PIP resolution is 0.1 mm and the minimum detectable particle diameter is approximately 0.3 mm (Newman et al., 2009). The smallest diameter bin used in calculations is 0.25 mm to 0.5 mm during BAECC and 0.2 mm to 0.4 mm in the following winter.

The PSD parameters were calculated using method of moments and assuming that PSD follows gamma functional form, see for example Ulbrich and Atlas (1998) and citations therein. The normalized gamma distribution $N(D)$ in $\text{mm}^{-1}\text{m}^{-3}$ was adopted following Testud et al. (2001); Bringi and Chandrasekar (2001); Illingworth and Blackman (2002):

$$N(D) = N_w f(\mu) \left(\frac{D}{D_0}\right)^{\mu} \exp(-\Lambda D) \tag{1}$$

$$f(\mu) = \frac{6}{3.67^4} \frac{(3.67+\mu)^{\mu+4}}{\Gamma(\mu+4)} \tag{2}$$

$$\Lambda = \frac{3.67+\mu}{D_0}, \tag{3}$$

with N_w in $\mathrm{mm}^{-1}\mathrm{m}^{-3}$ being the intercept parameter, D_0 the median volume diameter in mm, Λ the slope parameter in mm^{-1} and μ the shape parameter. Using the second, fourth and sixth moments for the non-truncated gamma PSD, M_2, M_4, and M_6, the PSD parameters were estimated as follows:

$$\eta = \frac{M_4^2}{M_6 M_2} \tag{4}$$

$$\mu = \frac{7 - 11\eta - \sqrt{\eta^2 + 14\eta + 1}}{2(\eta - 1)} \tag{5}$$

$$\Lambda = \sqrt{\frac{M_2 \Gamma(\mu+5)}{M_4 \Gamma(\mu+3)}} \tag{6}$$

$$D_0 = \frac{3.67+\mu}{\Lambda} \tag{7}$$

3.2 ~~Bulk~~ Ensemble mean density retrieval

The integration time, $\tau(t)$, of the ~~bulk~~ ensemble mean density retrieval is driven by precipitation measurements of the Pluvio^2. The step of the non-real-time accumulation output is 0.05 mm, causing the output interval to be in the order of several minutes even at moderate snow rates. With a short fixed integration time in time scales of minutes or tens of minutes, the produced ~~bulk~~ ensemble mean density estimation would hence be the more unstable, the lower the precipitation rate. Therefore, variable length time intervals driven by the gauge output are used with a selected threshold value of 0.1 mm. This corresponds to a $\tau(t)$ of 6 minutes for a LWE precipitation intensity of 1 mm h^{-1}. Effectively, the temporal resolution of the ensemble mean density retrieval is increased with increasing precipitation intensity, and in the analysis of the snowfall events in Table 1, the median $\tau(t)$ was 5 minutes.

As the integration time ~~interval~~ $\tau(t)$ is effectively driven by precipitation intensity, there is less variation in number of particles between intervals, compared to a fixed time interval approach. With the selected accumulation threshold there are typically between 10^3 and 10^4 particles within a given integration time interval. On the other hand, with low precipitation intensities, $\tau(t)$ increases up to one hour and retrieved ~~bulk density~~ $\bar{\rho}$ becomes less representative for the time interval in question. With LWE precipitation rates lower than 0.2 mm h^{-1}, the resolution of Pluvio^2 LWE measurements is insufficient and calculations of ~~bulk density~~ $\bar{\rho}$ become overly sensitive to recorded number concentrations. ~~Correspondinly~~Correspondingly, similar unwanted sensitivity to LWE precipitation accumulation occurs when the number of particles observed by PIP within $\tau(t)$ is less than 800. Therefore, time intervals with precipitation rates or particle counts lower than these thresholds are excluded from our analysis.

Given a population of solid precipitation particles with volume equivalent diameters D over the integration time $\tau(t)$, the liquid equivalent precipitation accumulation in mm is approximately

$$G(t) = \approx \frac{\pi}{6} \times 10^{-6} \frac{\rho}{\rho_w} \frac{\bar{\rho}}{\rho_w} \int_{t}^{t+\tau(t)} \int_{0 D_{min}}^{D_{max}} D^3 v(D,t) N(D,t) \, \mathrm{d}D\mathrm{d}t, \tag{8}$$

where ~~ρ~~ $\bar{\rho}$ is the volume flux weighted ~~snow bulk~~ population mean snow density in $\mathrm{g\,cm^{-3}}$, $\rho_w = 1\ \mathrm{g\,cm^{-3}}$ is the density of liquid water, $N(D,t)$ is mean particle number concentration over the integration time in $\mathrm{mm^{-1}m^{-3}}$ ~~and~~ , $v(D,t)$ is particle velocity relation in $\mathrm{m\,s^{-1}}$ and $[D_{min}, D_{max}]$ is the size range of snowflake observations from a disdrometer. From (8) we can ~~calculate snow bulk~~ estimate volume flux weighted snow density for each observation time interval as

$$\rho\bar{\rho}(t) = \approx \frac{6}{\pi} \times 10^{6} \rho_w \frac{G(t)}{\int_{t}^{t+\tau(t)} \int_{0}^{D_{max}} D^3 v(D,t) N(D,t) \, \mathrm{d}D\mathrm{d}t} \frac{G(t)}{\int_{t}^{t+\tau(t)} \int_{D_{min}}^{D_{max}} D^3 v(D,t) N(D,t) \, \mathrm{d}D\mathrm{d}t}, \tag{9}$$

using liquid equivalent precipitation accumulation $G(t)$ as measured by the Pluvio^2 gauge, and retrieving volume flux with fitted $v(D,t)$, and averaged $N(D,t)$ as measured by the PIP. It should be noted, that unlike in the retrieval of PSD parameters, where gamma PSD was assumed, ~~ρ~~ $\bar{\rho}$ was retrieved without making any assumptions on the shape of the PSD distribution, and instead, measured PSD are used in the calculations.

3.3 Comparison of derived mean density to snow depth observations

The definition of ~~bulk~~ ensemble mean density here is the same as for mean bulk density in B07. They determine the densities for 5-minute precipitation volumes derived with a 2DVD disdrometer observations together with precipitation mass measured by a weighing gauge. B07 defined the volume of a single particle by summing coin-shaped sub-volumes together estimated separately for both orthogonal projections and taking geometrical mean. As the ~~used diameter~~ diameter used in our study is the estimated volume-equivalent diameter, our results are comparable to B07. In Heymsfield et al. (2004), the volume of a single particle is defined as a function of circumscribing maximum diameter, and the population mean effective density is determined from ice water content (IWC). The estimated ~~bulk~~ ensemble mean snow density is volume-weighted and expected to have lower values than the velocity-weighted ~~bulk~~ snow density. The difference is not generally prominent especially with low-density aggregates, whose velocity-dimensional dependence is weak.

It should be noted that the derived density is inversely proportional to the snow ratio, R_s, assuming that issues related to packing of snowflakes on the ground can be ignored. The snow ratio (Power et al., 1964; Ware et al., 2006) is used by operational weather services to estimate change in snow depth from LWE observations and can be defined as follows:

$$R_s(t) = \frac{\rho_w}{\rho(t)} \frac{1}{P \cdot C} \frac{\rho_w}{\bar{\rho}(t)} \tag{10}$$

where ~~$\rho(t)$~~ $\bar{\rho}(t)$ is the volume flux weighted ~~bulk~~ snow density derived as shown in (9). ~~Given this connection~~, P is the packing efficiency of snowflakes and C is the snow compression. Assuming that the packing and compression terms, or their product

are close to unity, the derived density can be ~~used to verify~~ tested against the commonly used assumption that 1 mm of LWE accumulation corresponds to 1 cm change in snow depth. In Fig. 4 the combined distribution of estimated snow ratios on temporal scales defined by the gauge accumulation for all the 23 events analyzed in this study is shown. It can be seen that the mean and median values, equal to 10 and 9 respectively, are very close to the commonly assumed value. ~~This supports the validity of the retrieved bulk density values~~

This analysis assumes that packing efficiency of snowflakes is 100 % and compression of snow on the ground can be ignored, or snow compression counteracts reduction in snow density due to packing. The packing efficiency of snowflakes on the ground is not known. Random packing of the same size spheres has density of 64 % and dense packing of such spheres uses 74 % of the volume, corresponding to $P = 0.64$ and 0.74 respectively. Packing efficiency of equal spheroids depends on axis ratios and exceeds this of spheres and could exceed 77 % (Donev et al., 2004) . It is not unreasonable to expect that irregular shaped particles of variable sizes, such as snowflakes, would pack more efficiently than equal spheroids. At least, packing efficiency in excess of 90 % can be expected for spheres of several radii (de Laat et al., 2014) . The packing efficiency of 70 % would mean that density of freshly fallen snow would be 30 % lower than this of falling snowflakes. The packing efficiency of 80 % would correspond to 20 % bias in estimated snowflake density from snow depth measurements, or in 25 % underestimation of the snow depth change by using $\bar{\rho}(t)$. We don't know the exact value of the snow packing, but could expect that in the worst case scenario it is about 70 % and probably closer to 80 % or even higher. It should also be noted that the snow compression would counteract this, but we are considering only freshly fallen snow and expect that the compression factor C is very close to unity.

One of the major uncertainties in the density retrieval is the assumption about particle volume. In this study we have assumed that snowflakes are spheroids with axis ratios of 0.6. Given this assumption, a conversion factor relating volume equivalent and observed disc equivalent diameters was defined. ~~It should be noted that the volume flux, defined in the denominator of (9), is nothing more than rate of snow depth change~~Fig. 2 shows that for a reasonable range of ellipsoid axis ratios this conversion factor can range between 0.8 and 1. This range of values implies that the uncertainty in the density estimation can range from an overestimation by as much as 50 % to an underestimation by about 20 %. This range of uncertainty is much larger than what is expected from a comparison of the retrieved volume-flux weighted density and snow depth measurements, as was discussed above. Therefore, by comparing the PIP derived and the directly measured snow depths, the validity of the derived ~~bulk density values~~ values of $\bar{\rho}$, and assumption of particle shape, can be checked. In Fig. 5 hourly change in the snow depth measured by the Jenoptik SHD30 is compared to the PIP derived snow depth. It can be seen that the agreement is ~~rather goodand there are no systematic differences~~good, with RMSE of 0.30 cm, linear correlation coefficient of 0.88 and normalized bias as low as -0.06. This comparison also gives confidence about the validity of the derived ~~bulk~~ ensemble mean densities.

3.4 Effect of PSD truncation on derived ensemble mean snow density

The observed PSD are truncated on left and right sides (Ulbrich and Atlas, 1998) . They are truncated on the right side because of the instrument finite sampling volume and because natural sizes of hydrometeors do not extend to infinity. The truncation on the left, on the small-diameter side, is due to instrumental limitations and possible wind effects (Moisseev and Chandrasekar, 2007) .

Ulbrich and Atlas (1998) have presented a comprehensive analysis on how the right-side truncation affects the derived Gamma PSD parameters. A similar study on the effects of the left-side truncation and other instrumental effects was presented by Moisseev and Chandrasekar (2007) . Here we apply the method presented by Moisseev and Chandrasekar (2007) to estimate impact of PSD truncation on the derived mean snow density.

To investigate the impact of the PSD truncation on retrieval of mean snow density a simulation study was performed. To initiate the simulation the PSD parameters N_w, D_0 and μ, together with parameters of m-D and v-D are used. During the study it was found that the density estimation error is most sensitive to D_0 and μ and virtually independent of the other input parameters. Therefore, results presented here assume that N_w is constant and equal to 10^4 mm^{-1}m^{-3}, only one m-D relation representative of all BAECC cases, as presented in Section 4.3.1, is selected and v-D representative of the snowfall with mean density ranging between 100 and 200 g cm^{-3} is utilized. The D_0 values were varied between 0.5 and 4 and μ values between -0.9 and 3.

At the first stage of simulation a number of observed particles were computed assuming that it follows a Poisson distribution and the expected number of particles is determined by PIP sampling volume and the integration time that is determined by the precipitation accumulation. Given this number of particles, their diameters were found by sampling a Gamma probability density function, parameters of which are determined by the input PSD. To simulate the left-side truncation all particles with diameters smaller or equal to 0.25 mm, the PIP sensitivity threshold, were rejected. The right-side truncation was achieved by rejecting particles with sizes exceeding $3D_0$. For each D_0 and μ pair 50 simulated PSD were computed. Given the simulated truncated PSD the density is estimated in the same way as was presented above. This estimated density is compared to the one that is directly derived from the simulation input parameters and the results of their comparison is shown in Fig. 6. As one can see, the derived ensemble mean snow density is biased. The bias is largest for small D_0, which is explained by the left-side PSD truncation. For D_0 larger than 1 mm the bias decreases and approaches 2 %. Given that the error associated with PSD truncation is rather small, at least for D_0 larger than 1 mm and most of our observation fall within this range, in this study the truncation error is not corrected.

3.5 Velocity-dimensional analysis

For the retrieval of volume flux weighted snow density, velocity-dimensional relations of falling snow need to be estimated. For each integration time interval, $v(D) = a_v D^{b_v}$ is ~~computed~~fitted for velocity-diameter data from the PIP. The $v(D)$ power law fits to unfiltered data tend to be strongly biased by outliers. To address this problem, Gaussian kernel density estimation (KDE, Silverman, 1986) is used to find the most probable velocity for each diameter bin, and only observations with velocities within half width at half maximum from the bin peak KDE value are included in calculating the fit. Using the linear least squares method, a fit is performed for the data points in log-log scale to derive a power law relation. ~~Velocity fits retrieved this way~~ It should be noted, that using linear regression in log-log space does not optimally minimize residuals in linear space, but the method is used here as it does not overly emphasize the large end of the size spectrum. The retrieved velocity fits are shown for selected integration time intervals of the 18 March 2014 and the 22-23 January 2015 cases in the bottom of Figures 7 and 8, respectively.

It should be noted that the power law model, albeit widely used, may not necessary represent correctly velocities of ice particles over the complete range of diameters (Mitchell and Heymsfield, 2005). In many cases the fit can also be uncertain either because of narrow PSD or in presence of multiple particle types.

4 Results

4.1 Case studies

4.1.1 18 March 2014

During the March 18, Finland was covered in a continental polar air mass. In the morning, a warm occluded front associated with a weak low pressure center approached southern Finland from southwest bringing light snowfall. In the afternoon Hyytiälä was in the warm sector of the frontal system, and the relative humidity dropped halting the snowfall around 12 UTC. Later in the evening there was a one-hour snow shower from a squall line associated with a cold front passing over southern Finland.

Time series of LWE snow rate, ~~snow bulk~~ ensemble mean density and PSD parameters for the March 18 case are shown in Fig. 7. The bottom panels show measured fall velocities for selected integration time intervals representing observations with different ~~bulk~~ ensemble mean densities. Between the red dotted lines is the region where KDE is higher than half maximum for a given particle size. The fits are applied for data points between these lines. There is considerable scatter in particle fall velocity throughout the case and a bimodal PSD is present momentarily in the morning as can be seen in fall velocity panel Fig. 7a.

During the snow shower in the evening, liquid equivalent precipitation rates were recorded on average roughly three times more intense than earlier during the day~~were recorded~~, allowing retrievals of ~~bulk density~~ $\bar{\rho}$ and PSD parameters at high time resolutions. Strong short time scale variations of ~~ρ~~ $\bar{\rho}$ and PSD parameters are recorded during this shower. The lowest ~~bulk~~ ensemble mean density value of the case, 0.035 g cm^{-3}, is retrieved for time interval from 16:35 to 16:39, with concurrent D_0 value of 5.5 mm and N_w of roughly 700 mm^{-1}m^{-3}. The corresponding fall velocity distribution visualized in panel 7b is characterized by low values of velocity fit coefficients a_v and b_v. Within the following 20 minutes, D_0 decreases down to roughly 2 mm, N_w increases to 2×10^4 mm^{-1}m^{-3}, and retrieved values of ~~ρ~~ $\bar{\rho}$ peak at over 0.2 g cm^{-3} between 16:54 and 16:58, and again from 17:05 to 17:08. Corresponding fall velocity distribution between 16:54 and 16:56, shown in panel 7c, is characterized by substantially higher values of a_v and b_v, than 20 minutes earlier.

4.1.2 22-23 January 2015

During 22 January 2015, similarly to the 18 March 2014 event, a warm occluded front associated with a weak low moved northwards over the Gulf of Finland. However, due to a blocking high over north-western Russia, the low and the associated front were sustained over southern Finland for the whole day of January 23rd causing weak continuous precipitation in the area.

Time series of LWE snow rate, ~~bulk density~~ $\bar{\rho}$ and PSD parameters for the 22-23 January 2015 case, with velocity-diameter fits from selected time intervals are shown in Fig. 8. The case is characterized by continuous snowfall at LWE precipitation rates lower than 1 mm h^{-1} throughout the case. The velocity distribution for a given time interval has substantially less scatter compared to the 18 March 2014 case. The evolution of ~~ρ~~ $\bar{\rho}$ and N_w, as shown in Fig. 8, show considerable similarities, suggesting a strong correlation.

The velocity-diameter fits shown represent a low ~~bulk density ($\rho = 0.05\,\mathrm{g\,cm^{-3}}$~~ ensemble mean density ($\bar{\rho} = 0.05\,\mathrm{g\,cm^{-3}}$) time interval 01:03-01:16 (panel 8b) and two intervals 22:30-22:52 and 02:06-02:14 (8a, c) with higher ~~bulk densities~~ values of $\bar{\rho}$, 0.10 and 0.12 g cm^{-3}, respectively. Notable is the higher modal fall velocities and the absence of particles larger than 3 mm in the high density time intervals compared to the distribution in panel 8b.

4.2 v-D and density

In Fig. 9, particle fall velocity versus diameter data points combined from all the cases in Table 1 are divided into three categories according to the ~~bulk~~ snow ensemble mean density of the time interval during which particles were observed. A least squares fit is applied to observations in each ~~bulk density~~ $\bar{\rho}$ range using the same procedure as for velocity dimensional fits for integration time intervals, as described in section 3.5. The total number of observed particles is roughly 4,440,000, and for each ~~bulk~~ density category numbers of particles included in the fitting process (within the red lines in Fig. 9) are approximately 1,140,000, 1,190,000 and 360,000, respectively. The fitted relations for ~~bulk~~ ensemble mean density ranges are

$$v(D) = 0.834 D^{0.217}, \quad 0.0\,\mathrm{g\,cm^{-3}} < \rho\bar{\rho} \leq 0.1\,\mathrm{g\,cm^{-3}}, \tag{11}$$

$$v(D) = 0.895 D^{0.244}, \quad 0.1\,\mathrm{g\,cm^{-3}} < \rho\bar{\rho} \leq 0.2\,\mathrm{g\,cm^{-3}} \text{ and} \tag{12}$$

$$v(D) = 0.906 D^{0.256}, \quad \rho\bar{\rho} \geq 0.2\,\mathrm{g\,cm^{-3}}., \tag{13}$$

with RMSE values of 0.30 m s^{-1}, 0.30 m s^{-1} and 0.35 m s^{-1}, respectively.

The coefficient is increased with density indicating higher fall velocities with more dense particles. There is also a clear increase in the slope of the fitted curve from the lowest ~~bulk~~ density range to the $0.1 \ldots 0.2$ g cm^{-3} range indicated by the increase in the power term. With particles in the highest ~~bulk~~ density range the observed size distribution is narrow, hence the correlation between particle size and fall velocity is weak, and it is difficult to find an unambiguous relation between them. All things considered, the results are in line with the conclusion made by Barthazy and Schefold (2006), that the ~~constant~~ prefactor and power terms increase with riming degree, which in turn is strongly connected with density (Power et al., 1964) .

Considering the definition of the volume equivalent diameter, relations in the form of (11)…(13) should be ideal for velocity-dimensional parametrization of radar observations as the average size of hydrometeors as observed by radar are largely defined by their volumes rather than their shapes.

4.3 Connection between PSD parameters and density

From the analysis of PSD parameters and their relations to ~~bulk~~ ensemble mean density we have excluded data points representing integration time intervals where $D_0 < 0.6$ mm, as lower values of median volume diameter would imply that a substantial fraction of particles are too small to be observed with PIP. Applying this restriction, along with minimum thresholds set for particle count and LWE precipitation rate in density retrievals, as described in section 3.2, all in all 101 time intervals were discarded from the total of 1141 intervals of observations, leaving 7173 minutes of snow observations for the analysis.

4.3.1 Density and D_0

In Fig. 10, observed distributions of D_0 for the three different density regimes are shown. For the low density particles, the maximum D_0 value ~~does not seem to exceed 5…6~~ rarely exceeds 5 mm, which is in agreement with observations of snow aggregates presented by Lo and Passarelli (1982). It can also be seen that D_0 distribution depends on density. Low density particles are generally larger and vice versa. This dependence of D_0 on ~~bulk~~ ensemble mean density is not surprising, given that they are related as was previously shown by B07 and discussed in more detail below.

Relation between ~~snow bulk density~~ $\bar{\rho}$ and size (D_0) is illustrated in Fig. 11. The areas of individual data points are proportional to the particle counts of the corresponding observation time intervals. The overlaid black solid curve, a least squares fit applied for all cases in Table 1 is given by

$$\rho\bar{\rho}(D_0) = 0.226 D_0^{-1.004}, \tag{14}$$

where D_0 is in millimeters and ~~ρ~~ $\bar{\rho}$ is in g cm^{-3}. As the two examined winters were seen to have notable differences between each other in the snowfall type and average ~~bulk density~~ $\bar{\rho}$, corresponding relations were also calculated separately for the winters, and are given by

$$\rho\bar{\rho}(D_0) = 0.273 D_0^{-0.998} \quad \text{and} \tag{15}$$

$$\rho\bar{\rho}(D_0) = 0.209 D_0^{-0.969} \tag{16}$$

for BAECC events and for events of winter 2014/15, respectively. A relation by B07, given by ~~$\rho(D) = 0.178 D_0^{-0.922}$~~ $\bar{\rho}(D) = 0.178 D_0^{-0.922}$, is plotted in Fig. 11 for comparison. As their definitions of particle diameter and ~~bulk density~~ $\bar{\rho}$ are close to ours, the relations are easy to compare. Especially (16) is in good agreement with B07's results. The ~~bulk~~ ensemble mean density is on average higher for snow events recorded during BAECC, which suggests more riming occurred during those events. Indication to this is that the ARM AMF2 dual-channel microwave radiometer located on the same measurement field detected the presence of liquid water more than 80 % of the BAECC SNEX campaign time (Petäjä et al., 2016) and the presence of supercooled liquid layers could also be observed in the backscatter coefficient and circular depolarization ratio measurements of the co-located ARM HSRL (High Spectral Resolution Lidar) in the majority of the BAECC cases (Goldsmith et al., 2014). In general the BAECC winter was milder than the next winter 2014–2015, and the case duration weighted average of maximum recorded

temperatures was almost one degree higher for BAECC events compared to the value for winter 2014–2015 cases. The temperatures closer to 0°C could mean increased aggregation as stated in B07 and therefore decreased density values, but also different snow habits compared to ~~more~~ colder cases.

The mass-dimensional relation in power-law format ~~$m = a_m D_m^b$ can be induced~~ $m = a_m D^{b_m}$ can be derived from the retrieved ~~ρ~~$\bar{\rho}$-D_0 relations (14) to (16) by assuming ~~exponential~~ gamma PSD and describing the ~~bulk density as~~ ensemble mean density approximately as

$$\bar{\rho} = \frac{\int m(D)v(D)N(D)\mathrm{d}D}{\int V(D)v(D)N(D)\mathrm{d}D} \approx \frac{\int_0^\infty m(D)v(D)N(D)\mathrm{d}D}{\int_0^\infty V(D)v(D)N(D)\mathrm{d}D} \tag{17}$$

$$= \frac{\int a_m(D)^{b_m} a_v D^{b_v} N_0 \exp(-\Lambda D)\mathrm{d}D}{\int \frac{\pi}{6}(0.1D)^3 a_v D^{b_v} N_0 \exp(-\Lambda D)\mathrm{d}D} \frac{\int_0^\infty a_m(D)^{b_m} a_v D^{b_v} N_0 D^\mu \exp(-\Lambda D)\mathrm{d}D}{\int_0^\infty \frac{\pi}{6}(0.1D)^3 a_v D^{b_v} N_0 D^\mu \exp(-\Lambda D)\mathrm{d}D} \tag{18}$$

$$= \frac{6}{\pi}\frac{6}{\pi}10^3 a_m \frac{\Gamma(b_m + b_v + 1)}{\Gamma(4 + b_v)} D_0^{b_m - 3} \frac{\Gamma(b_m + b_v + \mu + 1)}{\Gamma(b_v + \mu + 4)} \left(\frac{0.1}{3.67}\frac{1}{3.67}\right)^{b_m - 3} D_0^{b_m - 3}. \tag{19}$$

The integration limits are defined from zero to infinity for deriving the analytic solution, though the true range is narrower because of left and right truncation of the observed size spectrum. As shown in Fig. 6, the ensemble mean density is overestimated because of the truncation. The estimation bias of density is ranging between 20 % for D_0 smaller than 0.75 mm and about 2 % for D_0 larger than 2 mm. Since for the estimation of the m-D relation, most of the observed D_0 values are higher than approx. 1 mm as shown in Fig. 10, there is only minor contribution of the smaller D_0 values, and we are assuming our error in ensemble mean density because of truncation to be close to 2 %. This corresponds to an error of 2 % also in the prefactor a_m, if assumed that the truncation does not introduce significant changes in the exponents of the $\bar{\rho}$-D_0 and m-D relations.

Taking the three velocity exponents from equations (11) to (13), and assuming exponential PSD, the derived prefactors and exponents of mass-relation ~~in grams~~ are shown in Table 2, having the volume-equivalent diameter proxy in mm and mass given in grams. The factor 0.1 in (18) derives from unit conversion, as ~~bulk density~~ $\bar{\rho}$ is in g cm^{-3}. The values of prefactor a_m are not sensitive to the changes in the velocity exponent b_v (changes in b_v are resulting less than 1 % devition a_m values), though there is a small increase in a_m with increasing b_v. The prefactor is more sensitive to shape parameter μ of the gamma PSD, the value of a_m increases by 24 % as μ is increased from zero to 1. With value of $\mu = 3$ the increase in the prefactor a_m value is 48 %. The shape factor of snow PSD is known to be noisy and thus often exponential distribution is assumed. With $b_v = 0.217$ the derived mass-dimensional relations for all cases and for both studied winters separately are plotted against literature values in Fig. 12. The derived exponent b_m for the studied cases is in line with literature values, close to 2, but the prefactor a_m values are higher than in the presented relations in Table 3. The highest value of a_m is for the BAECC cases indicating conditions of riming. The high prefactor values might manifest the Finnish winter conditions, because of the vicinity of Baltic Sea, the air is more moist than e.g. in continental conditions.

4.3.2 N_w and density

Distributions of observed N_w values also exhibit dependence of N_w on the ~~bulk~~ ensemble mean density, as shown in Fig. 13, i.e. N_w increases with density. The modal values of N_w are approximately 5000, 40,000 and 80,000 $\mathrm{mm^{-1}m^{-3}}$ for ~~bulk~~ ensemble mean density ranges $0.0 \ldots 0.1$, $0.1 \ldots 0.2$ and >0.2 $\mathrm{g\,cm^{-3}}$, respectively, with vast majority of N_w values spanning less than two orders of magnitude for a given ~~ρ~~ $\bar{\rho}$ range. This dependence of N_w on density is somewhat unexpected. There is no obvious reason to expect that N_w would depend on density. However, because D_0 and density are related, dependence of N_w on density potentially arises from the dependence of N_w on D_0.

To verify this, the partial correlation analysis of the relation between log values of N_w and density while controlling for log value of D_0 was carried out. It was found that there is a moderate negative partial correlation, -0.33, between N_w and density while controlling for D_0. However, the zero-order correlation between N_w and density is 0.52. The analysis confirms that the observed relation between N_w and density, is due to their relation to D_0. It is not clear, however, what is the meaning of the found negative partial correlation between N_w and density.

A relation between N_w and snow particle size is shown in Fig. 14a. A linear least squares fit is applied for $(D_0, \log(N_w))$, and the corresponding relation between N_w and D_0 is given by

$$N_w = 2.492 \times 10^5 \times 10^{-0.620 D_0}. \tag{20}$$

Bringi and Chandrasekar (2001) show that there is a weak tendency for N_w to decrease with increasing D_0 for rain (their Fig. 7.17), but to our knowledge, this is the first attempt to find a climatological relation between D_0 and N_w for snow. It should be noted, however, that the observed relation is partially caused by data filtering which removes low precipitation rate data. There is a high amount of scatter when $N_w < 1 \times 10^3\ \mathrm{mm^{-1}m^{-3}}$. The data points in this area are more contained when D_0 is multiplied with ~~$\rho^{1/3}$~~ $\bar{\rho}^{1/3}$ as shown in Fig. 14b. Making a fit to the resulting data points gives

$$N_w = 7.072 \times 10^5 \times 10^{-1.783 D_0 \rho^{1/3} - 1.783 D_0 \bar{\rho}^{1/3}}. \tag{21}$$

However, the difference in correlation coefficients for the fits in Figures 14a and b, given by -0.87 and -0.85, respectively, is minimal. The lower scatter in Fig. 14b for N_w in the sub $10^3\,\mathrm{mm^{-1}m^{-3}}$ range seems to be compensated by slightly more scatter in the higher end of the distribution.

4.3.3 PSD shape parameter, μ

In Fig. 15 the normalized frequencies of the gamma PSD shape factor μ are visualized in the three ~~bulk~~ ensemble mean density ranges. Unlike D_0 and N_w, μ does not seem to have a clear correlation with ~~snow bulk~~ ensemble mean snow density, although, a weak tendency for μ to increase with density is possible. Instead, the values of μ are scattered around approximately zero, with deviation increasing with density. In the ~~bulk~~ ensemble mean density ranges 0.0 to 0.1 and 0.1 to 0.2 $\mathrm{g\,cm^{-3}}$ the kernel densities peak at -0.15 and 0.62, with standard deviations of 0.97 and 1.58, respectively. For the integration intervals with ~~$\rho > 0.2\ \mathrm{g\,cm^{-3}}$~~ $\bar{\rho} > 0.2\ \mathrm{g\,cm^{-3}}$, the distribution of μ is more spread, with standard deviation of 2.0 and median of 0.76. The

observations support the findings of B07 and ~~?~~ Heymsfield et al. (2008) , who have found that low density particles generally have exponential or slightly super-exponential distributions. This suggests, the exponential PSD would be most appropriate for describing low density aggregated snow and less so when strong riming occurs.

5 Conclusions

Microphysical properties of snow in Southern Finland were documented using observations from PIP and a weighing gauge. The data was collected during US DOE ARM funded BAECC campaign and the consecutive winter. It is shown that there is a detectable difference in measured snow properties between ~~the two~~ consecutive winters. Snow observed during BAECC is denser than during the next winter. The derived m-D relations from two winters are also different, and the difference is namely in the prefactor of the power law relations.

It is found that D_0 and N_w parameters of Gamma PSD are correlated with ~~the bulk density~~ $\bar{\rho}$. While the relation between ~~bulk~~ ensemble mean density and D_0 is not surprising, since these two parameters are related, the correlation between N_w and ~~bulk density~~ $\bar{\rho}$ is interesting. This correlation arises from the observed connection between N_w and D_0. It should be noted that this observed connection is partially due to data filtering that removes low precipitation rate data from the analysis. However, it indicates that for heavier precipitation aggregation is an important snow growth process. During snow growth by aggregation, N_w should decrease while D_0 increases, as was found by (Lo and Passarelli, 1982). The shape parameter of the Gamma PSD, μ, does not seem to depend on ~~bulk~~ ensemble mean density and its average value is close to zero, which is inline with studies reported in literature.

Dependence of v-D relation on ~~bulk~~ ensemble mean density was also studied. It was found that the prefactor of the v-D power law depends on density. It is higher for higher densities. This result is in agreement with the conclusion made by Barthazy and Schefold (2006), that the coefficient and power terms increase with riming degree.

The presented study uses the newly developed instrument Particle Imaging Package, which is a new generation of SVI . It is shown that data collected by this instrument is adequate for such studies. While the instrument only observes particle shapes projected to single 2D plane, as opposed to 2DVD or MASC, it has a larger sampling volume and its observations are less affected by wind (Newman et al., 2009). Additionally, the instrument itself is operationally more robust and requires less maintenance enabling deployment in sites with remote locations and harsh field conditions.

Acknowledgements. We would like to acknowledge the Hyytiälä station and University of Helsinki personnel for the daily tasks with measurements, especially mentioning Matti Leskinen and Janne Levula. The research of JT and DM was supported by Academy of Finland (grant 263333) and the Academy of Finland Finnish Center of Excellence program (grant 272041). AvL was funded by grant of the Vilho, Yrjö and Kalle Väisälä Foundation and by SESAR Joint Undertaking Horizon 2020 grant agreement No 699221 (PNOWWA). The instrumentation used in this study was supported by NASA Global Precipitation Measurement Mission ground validation program and by the Office of Science U.S. Department of Energy ARM program.

References

Aikins, J., Friedrich, K., Geerts, B., and Pokharel, B.: Role of a Cross-Barrier Jet and Turbulence on Winter Orographic Snowfall, Monthly Weather Review, 144, 3277–3300, doi:10.1175/MWR-D-16-0025.1, 2016.

Barthazy, E. and Schefold, R.: Fall velocity of snowflakes of different riming degree and crystal types, Atmospheric research, 82, 391–398, 2006.

Barthazy, E., Göke, S., Schefold, R., and Högl, D.: An Optical Array Instrument for Shape and Fall Velocity Measurements of Hydrometeors, Journal of Atmospheric and Oceanic Technology, 21, 1400–1416, doi:10.1175/1520-0426(2004)021<1400:AOAIFS>2.0.CO;2, 2004.

Brandes, E. A., Ikeda, K., Zhang, G., Schönhuber, M., and Rasmussen, R. M.: A statistical and physical description of hydrometeor distributions in Colorado snowstorms using a video disdrometer, Journal of applied meteorology and climatology, 46, 634–650, 2007.

Bringi, V. N. and Chandrasekar, V.: Polarimetric Doppler weather radar: principles and applications, Cambridge University Press, 2001.

Böhm, H. P.: A General Equation for the Terminal Fall Speed of Solid Hydrometeors, J. Atmos. Sci., 46, 2419–2427, doi:10.1175/1520-0469(1989)046<2419:AGEFTT>2.0.CO;2, http://dx.doi.org/10.1175/1520-0469(1989)046<2419:AGEFTT>2.0.CO;2, 1989.

de Laat, D., de Oliveira, F., Fernando, M., and Vallentin, F.: Upper bounds for packings of spheres of several radii, Forum of Mathematics, Sigma, 2, e23 (42 pages), doi:10.1017/fms.2014.24, http://journals.cambridge.org/article_S2050509414000243, 2014.

Dolan, B. and Rutledge, S. A.: A theory-based hydrometeor identification algorithm for X-band polarimetric radars, Journal of Atmospheric and Oceanic Technology, 26, 2071–2088, http://journals.ametsoc.org/doi/abs/10.1175/2009JTECHA1208.1, 2009.

Donev, A., Stillinger, F., Chaikin, P., and Torquato, S.: Unusually dense crystal packings of ellipsoids, Physical review letters, 2004.

Garrett, T. J. and Yuter, S. E.: Observed influence of riming, temperature, and turbulence on the fallspeed of solid precipitation, Geophysical Research Letters, 41, 6515–6522, doi:10.1002/2014GL061016, http://doi.wiley.com/10.1002/2014GL061016, 2014.

Garrett, T. J., Fallgatter, C., Shkurko, K., and Howlett, D.: Fall speed measurement and high-resolution multi-angle photography of hydrometeors in free fall, Atmos. Meas. Tech., 5, 2625–2633, doi:10.5194/amt-5-2625-2012, http://www.atmos-meas-tech.net/5/2625/2012/, 2012.

Goldsmith, J., Ermold, B., and Eloranta, E.: High Spectral Resolution Lidar (HSRL), ARM Mobile Facility (TMP), University of Helsinki Research Station (SMEAR II), Hyytiälä, Finland, doi:10.5439/1025200, 2014.

Hanesch, M.: Fall velocity and shape of snowflakes, Ph.D. thesis, Swiss Federal Institute of Technology, Zurich, 1999.

Heymsfield, A. and Westbrook, C.: Advances in the estimation of ice particle fall speeds using laboratory and field measurements, Journal of the Atmospheric Sciences, 67, 2469–2482, 2010.

Heymsfield, A. J., Bansemer, A., Schmitt, C., Twohy, C., and Poellot, M. R.: Effective Ice Particle Densities Derived from Aircraft Data, Journal of the Atmospheric Sciences, 61, 982–1003, doi:10.1175/1520-0469(2004)061<0982:EIPDDF>2.0.CO;2, 2004.

Heymsfield, A. J., Field, P., and Bansemer, A.: Exponential Size Distributions for Snow, Journal of the Atmospheric Sciences, 65, 4017–4031, doi:10.1175/2008JAS2583.1, 2008.

Huang, G.-J., Bringi, V. N., Cifelli, R., Hudak, D., and Petersen, W. A.: A Methodology to Derive Radar Reflectivity–Liquid Equivalent Snow Rate Relations Using C-Band Radar and a 2D Video Disdrometer, J. Atmos. Oceanic Technol., 27, 637–651, doi:10.1175/2009JTECHA1284.1, http://dx.doi.org/10.1175/2009JTECHA1284.1, 2010.

Huang, G.-J., Bringi, V., Moisseev, D., Petersen, W., Bliven, L., and Hudak, D.: Use of 2D-video disdrometer to derive mean density–size and Ze–SR relations: Four snow cases from the light precipitation validation experiment, Atmospheric Research, 153, 34–48, doi:10.1016/j.atmosres.2014.07.013, http://linkinghub.elsevier.com/retrieve/pii/S0169809514002762, 2015.

Iguchi, T., Matsui, T., Shi, J. J., Tao, W.-K., Khain, A. P., Hou, A., Cifelli, R., Heymsfield, A., and Tokay, A.: Numerical analysis using WRF-SBM for the cloud microphysical structures in the C3VP field campaign: Impacts of supercooled droplets and resultant riming on snow microphysics, Journal of Geophysical Research: Atmospheres, 117, http://onlinelibrary.wiley.com/doi/10.1029/2012JD018101/full, 2012.

Illingworth, A. J. and Blackman, T. M.: The Need to Represent Raindrop Size Spectra as Normalized Gamma Distributions for the Interpretation of Polarization Radar Observations, Journal of Applied Meteorology, 41, 286–297, doi:10.1175/1520-0450(2002)041<0286:TNTRRS>2.0.CO;2, http://dx.doi.org/10.1175/1520-0450(2002)041<0286:TNTRRS>2.0.CO;2, 2002.

Khvorostyanov, V. I. and Curry, J. A.: Fall Velocities of Hydrometeors in the Atmosphere: Refinements to a Continuous Analytical Power Law, Journal of the Atmospheric Sciences, 62, 4343–4357, doi:10.1175/JAS3622.1, 2005.

Kneifel, S., von Lerber, A., Tiira, J., Moisseev, D., Kollias, P., and Leinonen, J.: Observed relations between snowfall microphysics and triple-frequency radar measurements: TRIPLE-FREQUENCY SIGNATURES OF SNOWFALL, Journal of Geophysical Research: Atmospheres, pp. n/a–n/a, doi:10.1002/2015JD023156, http://doi.wiley.com/10.1002/2015JD023156, 2015.

Korolev, A. and Isaac, G.: Roundness and aspect ratio of particles in ice clouds, Journal of Atmospheric Sciences, 60, 1795–1808, 2003.

Leinonen, J., Moisseev, D., Leskinen, M., and Petersen, W. A.: A Climatology of Disdrometer Measurements of Rainfall in Finland over Five Years with Implications for Global Radar Observations, Journal of Applied Meteorology and Climatology, 51, 392–404, doi:10.1175/JAMC-D-11-056.1, http://dx.doi.org/10.1175/JAMC-D-11-056.1, 2012.

Lo, K. and Passarelli, Jr, R.: The Growth of Snow in Winter Storms:. An Airborne Observational Study, Journal of the Atmospheric Sciences, 39, 697–706, doi:10.1175/1520-0469(1982)039<0697:TGOSIW>2.0.CO;2, 1982.

Locatelli, J. D. and Hobbs, P. V.: Fall speeds and masses of solid precipitation particles, Journal of Geophysical Research, 79, 2185–2197, 1974.

Löffler-Mang, M. and Blahak, U.: Estimation of the equivalent radar reflectivity factor from measured snow size spectra, J. Appl. Meteor., 40, 843–849, doi:10.1175/1520-0450(2001)040<0843;EOTERR>2.0.CO;2, 2001.

Löffler-Mang, M. and Joss, J.: An optical disdrometer for measuring size and velocity of hydrometeors, Journal of Atmospheric and Oceanic Technology, 17, 130–139, doi:10.1175/1520-0426(2000)017<0130;AODFMS>2.0.CO;2, 2000.

Magono, C. and Nakamura, T.: Aerodynamic Studies of Falling Snowflakes, Journal of the Meteorological Society of Japan. Ser. II, 43, 139–147, 1965.

Matrosov, S., Reinking, R., and Djalalova, I.: Inferring fall attitudes of pristine dendritic crystals from polarimetric radar data, Journal of Atmospheric Sciences, 62, 241–250, doi:10.1175/JAS-3356.1, 2005a.

Matrosov, S. Y.: Variability of Microphysical Parameters in High-Altitude Ice Clouds: Results of the Remote Sensing Method, J. Appl. Meteor., 36, 633–648, doi:10.1175/1520-0450-36.6.633, http://dx.doi.org/10.1175/1520-0450-36.6.633, 1997.

Matrosov, S. Y.: Modeling Backscatter Properties of Snowfall at Millimeter Wavelengths, J. Atmos. Sci., 64, 1727–1736, doi:10.1175/JAS3904.1, http://dx.doi.org/10.1175/JAS3904.1, 2007.

Matrosov, S. Y., Heymsfield, A. J., and Wang, Z.: Dual-frequency radar ratio of nonspherical atmospheric hydrometeors, Geophysical Research Letters, 32, n/a–n/a, doi:10.1029/2005GL023210, http://dx.doi.org/10.1029/2005GL023210, l13816, 2005b.

Matrosov, S. Y., Campbell, C., Kingsmill, D., and Sukovich, E.: Assessing snowfall rates from X-band radar reflectivity measurements, Journal of Atmospheric and Oceanic Technology, 26, 2324–2339, http://journals.ametsoc.org/doi/abs/10.1175/2009JTECHA1238.1, 2009.

Mitchell, D. L.: Use of Mass- and Area-Dimensional Power Laws for Determining Precipitation Particle Terminal Velocities, J. Atmos. Sci., 53, 1710–1723, doi:10.1175/1520-0469(1996)053<1710:UOMAAD>2.0.CO;2, http://dx.doi.org/10.1175/1520-0469(1996)053<1710:UOMAAD>2.0.CO;2, 1996.

Mitchell, D. L. and Heymsfield, A. J.: Refinements in the Treatment of Ice Particle Terminal Velocities, Highlighting Aggregates, J. Atmos. Sci., 62, 1637–1644, doi:10.1175/JAS3413.1, http://dx.doi.org/10.1175/JAS3413.1, 2005.

Mitchell, D. L., Zhang, R., and Pitter, R. L.: Mass-Dimensional Relationships for Ice Particles and the Influence of Riming on Snowfall Rates, J. Appl. Meteor., 29, 153–163, doi:10.1175/1520-0450(1990)029<0153:MDRFIP>2.0.CO;2, http://dx.doi.org/10.1175/1520-0450(1990)029<0153:MDRFIP>2.0.CO;2, 1990.

Moisseev, D. N. and Chandrasekar, V.: Examination of the mu–Lambda Relation Suggested for Drop Size Distribution Parameters, J. Atmos. Oceanic Technol., 24, 847–855, doi:10.1175/JTECH2010.1, http://dx.doi.org/10.1175/JTECH2010.1, 2007.

Morrison, H. and Milbrandt, J. A.: Parameterization of Cloud Microphysics Based on the Prediction of Bulk Ice Particle Properties. Part I: Scheme Description and Idealized Tests, J. Atmos. Sci., 72, 287–311, doi:10.1175/JAS-D-14-0065.1, http://dx.doi.org/10.1175/JAS-D-14-0065.1, 2015.

Newman, A. J., Kucera, P. A., and Bliven, L. F.: Presenting the Snowflake Video Imager (SVI), Journal of Atmospheric and Oceanic Technology, 26, 167–179, doi:10.1175/2008JTECHA1148.1, http://journals.ametsoc.org/doi/abs/10.1175/2008JTECHA1148.1, 2009.

Petäjä, T., O'Connor, E. J., Moisseev, D., Sinclair, V. A., Manninen, A. J., Väänänen, R., von Lerber, A., Thornton, J. A., Nicoll, K., Petersen, W., Chandrasekar, V., Smith, J. N., Winkler, P. M., Krüger, O., Hakola, H., Timonen, H., Brus, D., Laurila, T., Asmi, E., Riekkola, M.-L., Mona, L., Massoli, P., Engelmann, R., Komppula, M., Wang, J., Kuang, C., Bäck, J., Virtanen, A., Levula, J., Ritsche, M., and Hickmon, N.: BAECC A field campaign to elucidate the impact of Biogenic Aerosols on Clouds and Climate, Bull. Amer. Meteor. Soc., doi:10.1175/BAMS-D-14-00199.1, http://dx.doi.org/10.1175/BAMS-D-14-00199.1, 2016.

Power, B. A., Summers, P. W., and D'Avignon, J.: Snow Crystal Forms and Riming Effects as Related to Snowfall Density and General Storm Conditions, J. Atmos. Sci., 21, 300–305, doi:10.1175/1520-0469(1964)021<0300:SCFARE>2.0.CO;2, http://dx.doi.org/10.1175/1520-0469(1964)021<0300:SCFARE>2.0.CO;2, 1964.

Pruppacher, H. and Klett, J.: Microphysics of Clouds and Precipitation, Atmospheric and Oceanographic Sciences Library, Springer Netherlands, https://books.google.fi/books?id=1mXN_qZ5sNUC, 1996.

Rasmussen, R., Baker, B., Kochendorfer, J., Meyers, T., Landolt, S., Fischer, A. P., Black, J., Thériault, J. M., Kucera, P., Gochis, D., Smith, C., Nitu, R., Hall, M., Ikeda, K., and Gutmann, E.: How Well Are We Measuring Snow: The NOAA/FAA/NCAR Winter Precipitation Test Bed, Bull. Amer. Meteor. Soc., 93, 811–829, doi:10.1175/BAMS-D-11-00052.1, http://dx.doi.org/10.1175/BAMS-D-11-00052.1, 2012.

Schönhuber, M., Lammer, G., and Randeu, W.: One decade of imaging precipitation measurement by 2D-video-distrometer, Advances in Geosciences, 10, 85–90, doi:10.5194/adgeo-10-85-2007, 2007.

Sekhon, R. S. and Srivastava, R. C.: Snow Size Spectra and Radar Reflectivity, J. Atmos. Sci., 27, 299–307, doi:10.1175/1520-0469(1970)027<0299:SSSARR>2.0.CO;2, http://dx.doi.org/10.1175/1520-0469(1970)027<0299:SSSARR>2.0.CO;2, 1970.

Silverman, B. W.: Density estimation for statistics and data analysis, vol. 26, CRC press, 1986.

Szyrmer, W. and Zawadzki, I.: Snow Studies. Part II: Average Relationship between Mass of Snowflakes and Their Terminal Fall Velocity, J. Atmos. Sci., 67, 3319–3335, doi:10.1175/2010JAS3390.1, http://dx.doi.org/10.1175/2010JAS3390.1, 2010.

Testud, J., Oury, S., Black, R. A., Amayenc, P., and Dou, X.: The Concept of "Normalized" Distribution to Describe Raindrop Spectra: A Tool for Cloud Physics and Cloud Remote Sensing, Journal of Applied Meteorology, 40, 1118–1140, doi:10.1175/1520-0450(2001)040<1118:TCONDT>2.0.CO;2, http://dx.doi.org/10.1175/1520-0450(2001)040<1118:TCONDT>2.0.CO;2, 2001.

Thompson, G., Field, P. R., Rasmussen, R. M., and Hall, W. D.: Explicit forecasts of winter precipitation using an improved bulk microphysics scheme. Part II: Implementation of a new snow parameterization, Monthly Weather Review, 136, 5095–5115, http://journals.ametsoc.org/doi/abs/10.1175/2008MWR2387.1, 2008.

Tokay, A., Wolff, D. B., and Petersen, W. A.: Evaluation of the New Version of the Laser-Optical Disdrometer, OTT Parsivel2, J. Atmos. Oceanic Technol., 31, 1276–1288, doi:10.1175/JTECH-D-13-00174.1, http://dx.doi.org/10.1175/JTECH-D-13-00174.1, 2014.

Tong, M. and Xue, M.: Simultaneous estimation of microphysical parameters and atmospheric state with simulated radar data and ensemble square root Kalman filter. Part I: Sensitivity analysis and parameter identifiability, Monthly weather review, 136, 1630–1648, http://journals.ametsoc.org/doi/abs/10.1175/2007MWR2070.1, 2008.

Ulbrich, C. W. and Atlas, D.: Rainfall Microphysics and Radar Properties: Analysis Methods for Drop Size Spectra, Journal of Applied Meteorology, 37, 912–923, doi:10.1175/1520-0450(1998)037<0912:RMARPA>2.0.CO;2, 1998.

Ware, E. C., Schultz, D. M., Brooks, H. E., Roebber, P. J., and Bruening, S. L.: Improving Snowfall Forecasting by Accounting for the Climatological Variability of Snow Density, Weather and Forecasting, 21, 94–103, doi:10.1175/WAF903.1, 2006.

Wood, N. B., L'Ecuyer, T. S., Bliven, F. L., and Stephens, G. L.: Characterization of video disdrometer uncertainties and impacts on estimates of snowfall rate and radar reflectivity, Atmospheric Measurement Techniques, 6, 3635–3648, doi:10.5194/amt-6-3635-2013, http://www.atmos-meas-tech.net/6/3635/2013/, 2013.

Woods, C. P., Stoelinga, M. T., and Locatelli, J. D.: The IMPROVE-1 Storm of 1–2 February 2001. Part III: Sensitivity of a Mesoscale Model Simulation to the Representation of Snow Particle Types and Testing of a Bulk Microphysical Scheme with Snow Habit Prediction, J. Atmos. Sci., 64, 3927–3948, doi:10.1175/2007JAS2239.1, http://dx.doi.org/10.1175/2007JAS2239.1, 2007.

Zhang, G., Luchs, S., Ryzhkov, A., Xue, M., Ryzhkova, L., and Cao, Q.: Winter precipitation microphysics characterized by polarimetric radar and video disdrometer observations in central Oklahoma, Journal of Applied Meteorology and Climatology, 50, 1558–1570, http://journals.ametsoc.org/doi/abs/10.1175/2011JAMC2343.1, 2011.

Figure 1. Snow precipitation instruments on the measurement field in ~~Hyytiala~~Hyytiälä. The Pluvio^2 200 is inside the wind protection on a platform and the PIP lamp can be seen at right on the ground. The view of the picture is to southwest and the distance from the platform to the treeline behind is approximately 20 m.

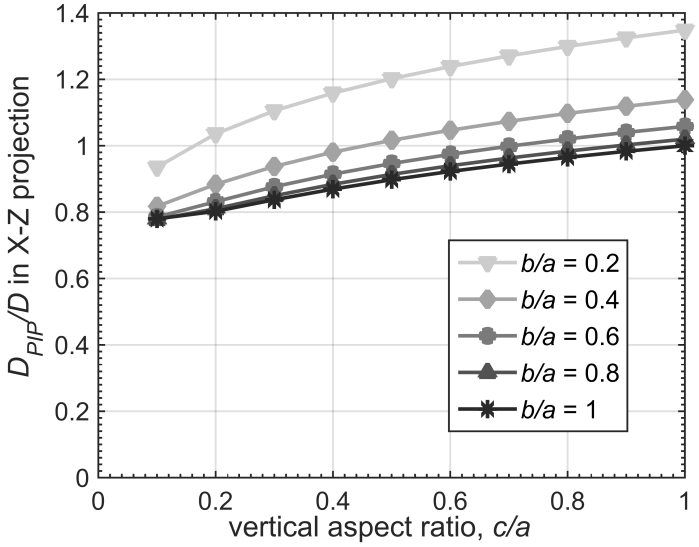

Figure 2. ~~Distribution of snow ratios,~~ The ratio of ~~snow depth change to LWE~~the diameter observed by PIP, ~~calculated from retrieved bulk densities~~D_{PIP}, to volume equivalent diameter D.

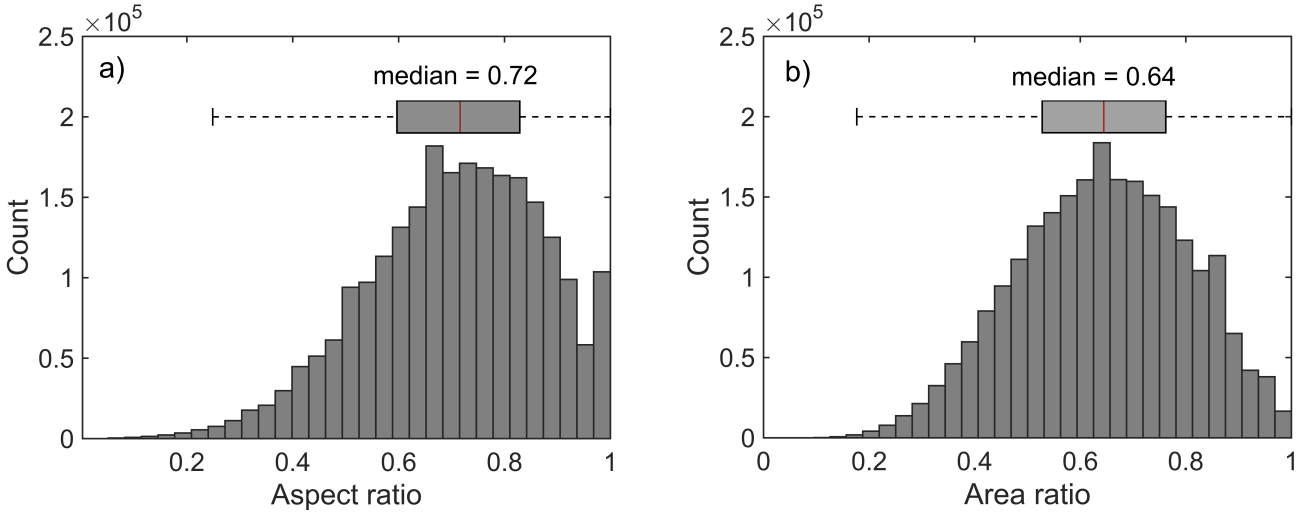

Figure 3. The distributions of snowflake a) aspect ratio and b) area ratio as observed using PIP with interquartile ranges visualized and median values shown.

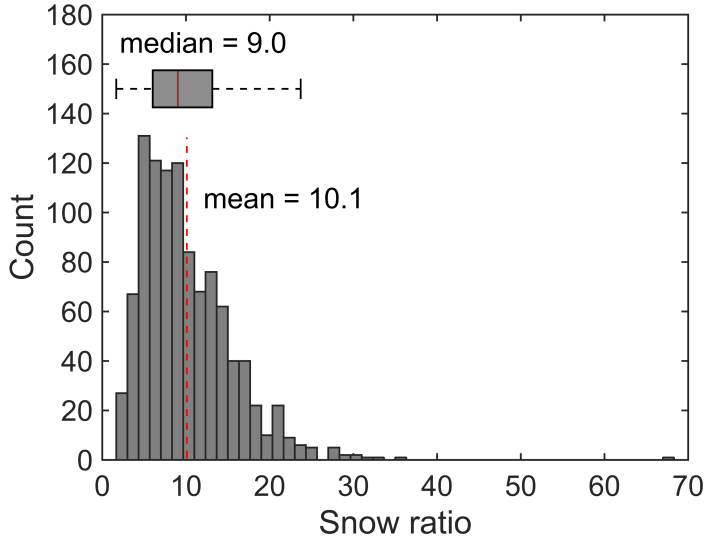

Figure 4. Distribution of snow ratios, ratio of snow depth change to LWE, calculated from retrieved ensemble mean densities with interquartile range, and median and mean values.

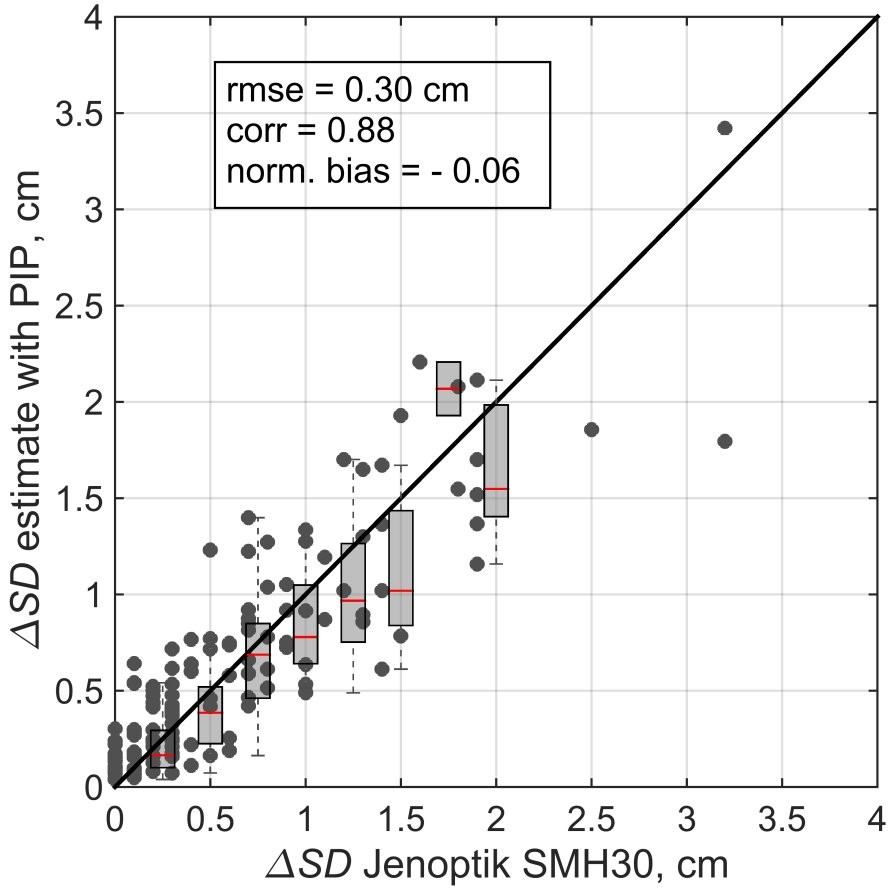

Figure 5. Scatterplot of the hourly change of snow depth measured with Jenoptik SMH30 and estimated from volume flux using PSD and fall velocities as measured by PIP. The data includes all the studied cases except Jan 10-11 2015.

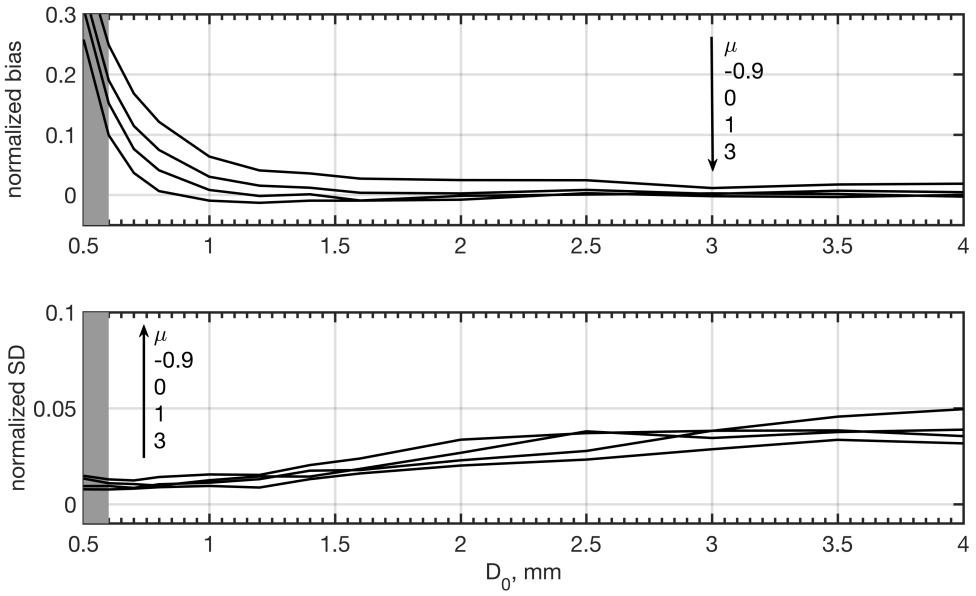

Figure 6. Computed normalized bias and standard deviation of estimated mean snow density as a function of μ and D_0. The shaded area indicates data that is not included in the analysis, because derived D_0 is smaller than 0.6 mm. The increased values of bias at low D_0 values is due to left side truncation of the observed PSD, which is caused by the instrument sensitivity. At larger D_0 values the bias approaches value of 0.02.

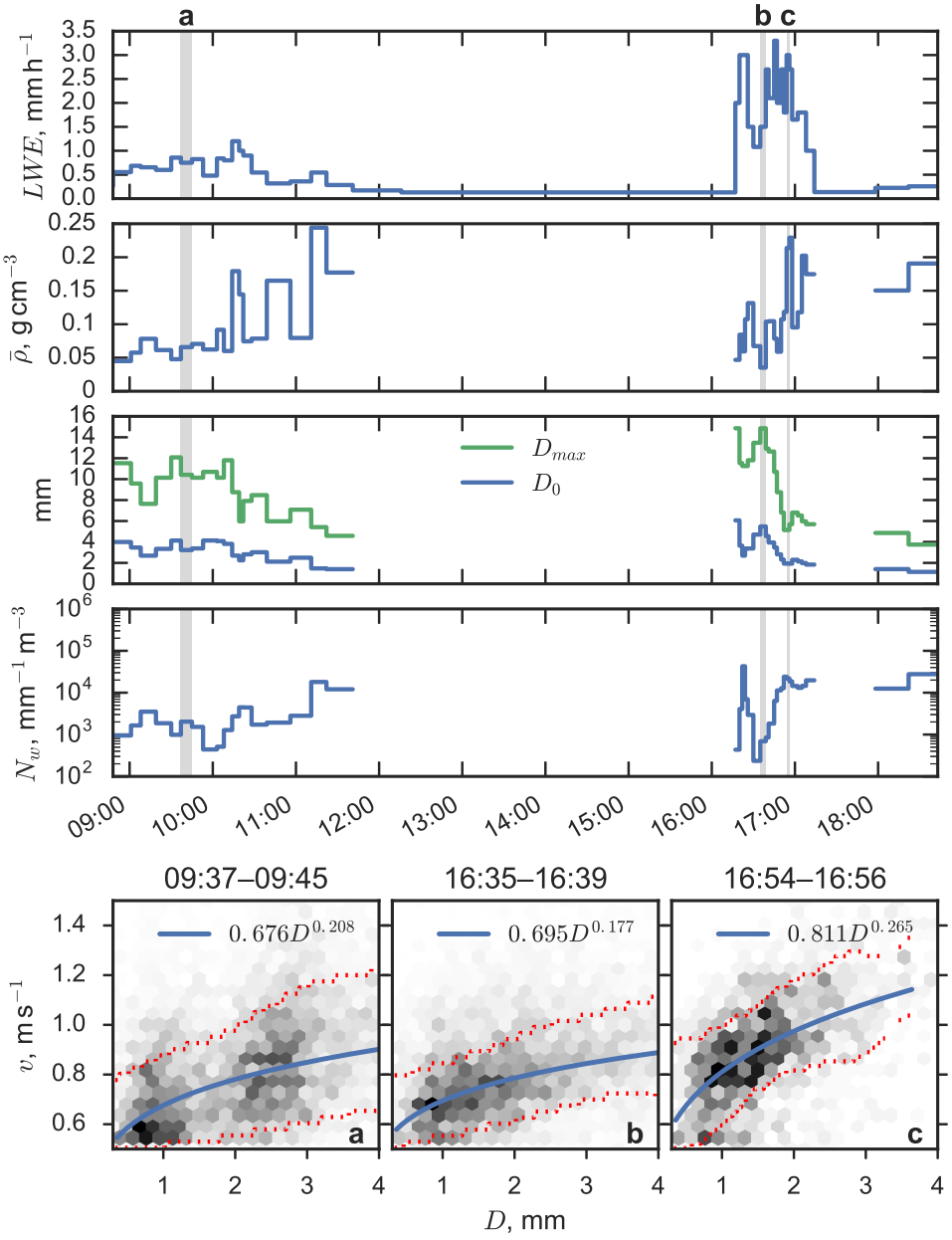

Figure 7. Evolution of snowfall intensity, ~~bulk~~ ensemble mean density and particle size distribution parameters during March 18th 2015 with associated (v, D) from three selected time intervals (highlighted in gray). The red dashed lines mark the upper and lower velocity limits where for a given D, the KDE value is higher than half maximum.

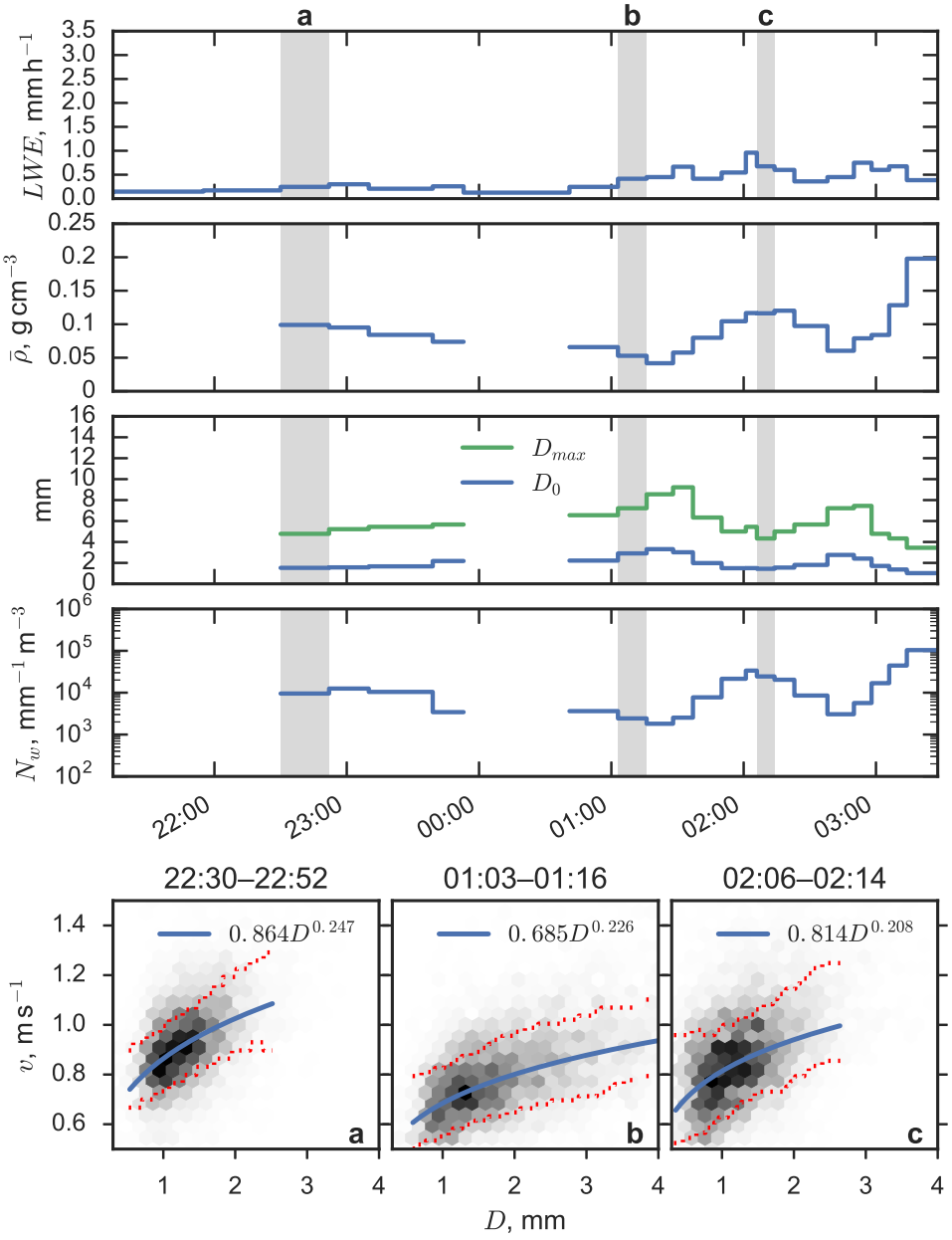

Figure 8. Evolution of snowfall intensity, ~~bulk~~ ensemble mean density and particle size distribution parameters during the night between the 22nd and 23rd of January 2015 with associated (v, D) from three selected time intervals (highlighted in grey). The red dashed lines mark the upper and lower velocity limits where for a given D, the KDE value is higher than half maximum.

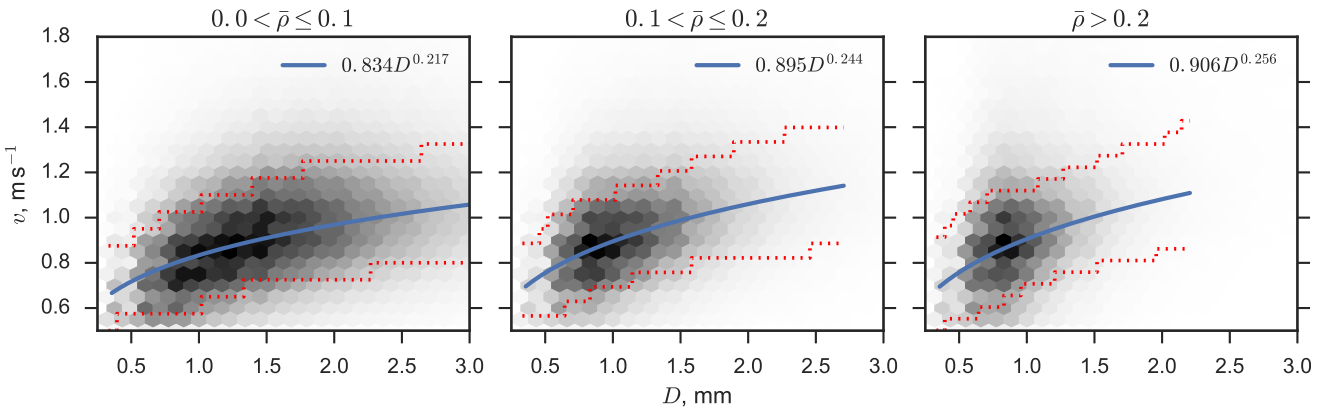

Figure 9. ~~Propability~~ Probability densities of (D, v) in three ~~bulk~~ ensemble mean density ranges ($[\bar{\rho}]$ = g cm^{-3}). Dashed lines mark the full width at half maximum KDE in each diameter bin. Power law functions are fitted for data between those lines.

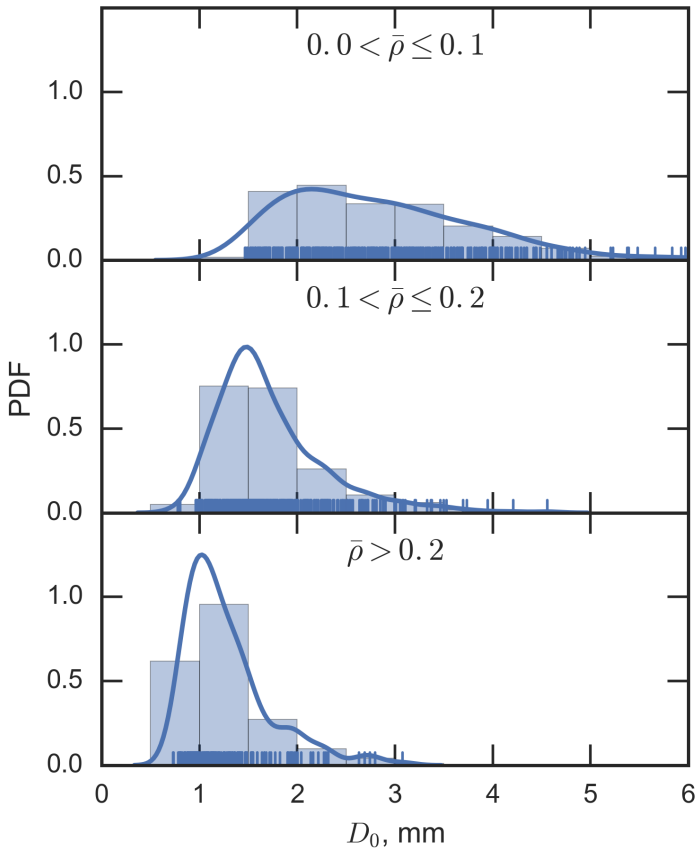

Figure 10. Normalized frequency (bars) and kernel density (line) of median volume diameter D_0 in three ~~bulk~~ ensemble mean density ranges, ~~$[\rho]$~~ $[\bar{\rho}]$ = g cm~~$^{-3}$~~$^{-3}$.

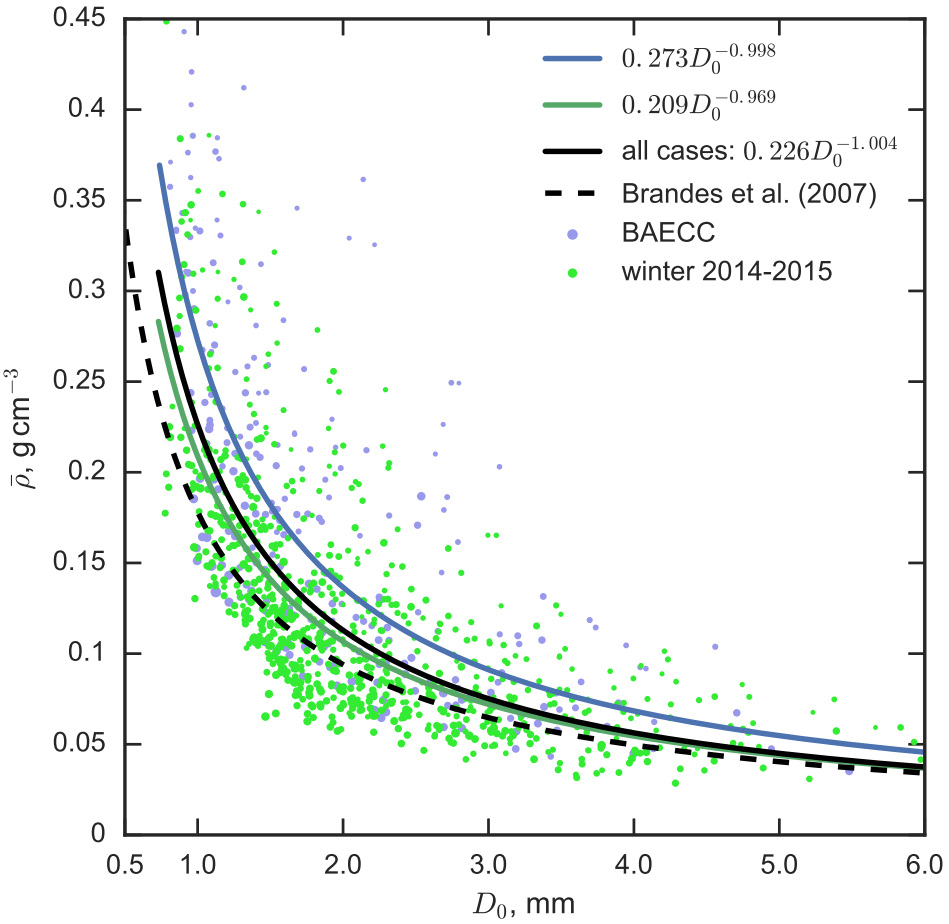

Figure 11. (D_0, ~~ρ~~$\bar{\rho}$) for all cases listed in ~~table~~ Table 1. Area of each dot is proportional to the number of particles in corresponding integration time interval. Power law fits are shown separately for BAECC winter cases (blue) and cases from the following winter (green).

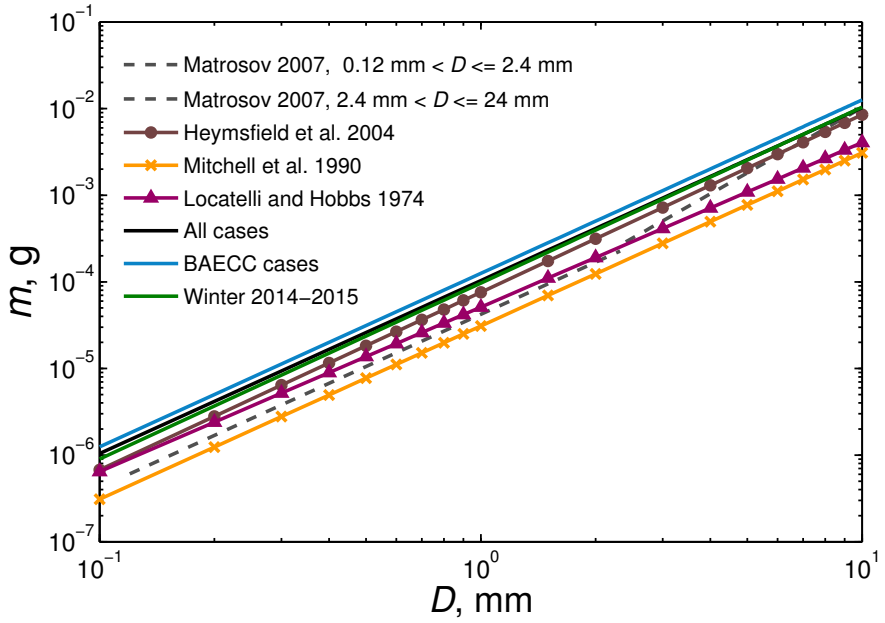

Figure 12. Derived m-D relations assuming exponential PSD in comparison relations presented in literature are shown in Table 3. ~~The~~ A conversion of maximum dimension to volume equivalent diameter is done by assuming axis ratio of 0.6.

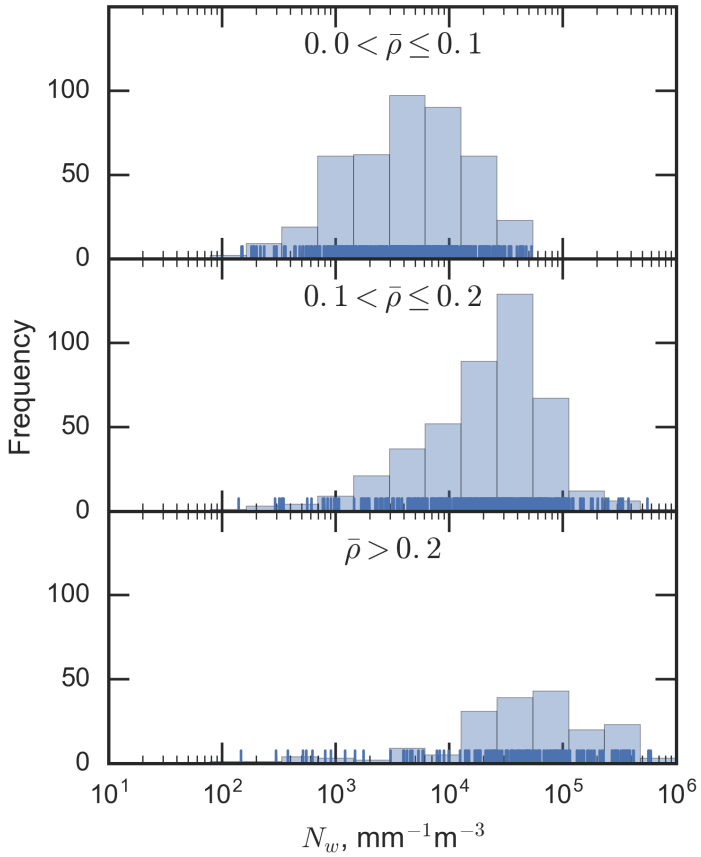

Figure 13. Frequency of N_w in three ~~bulk~~ ensemble mean density ranges, ~~[ρ]~~ [$\bar{\rho}$] = g cm~~$^{-3}$~~ $^{-3}$.

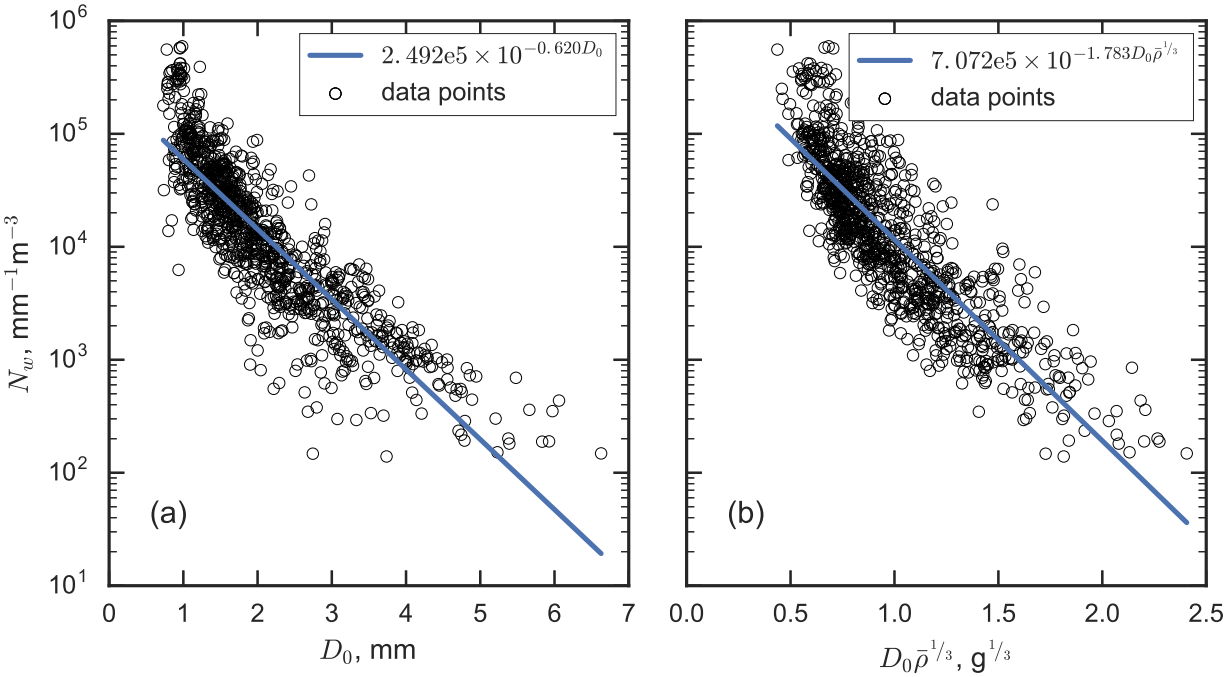

Figure 14. (D_0, N_w) and (~~$D_0\rho^{1/3}$~~ $D_0\bar{\rho}^{1/3}$, N_w) with fitted relations

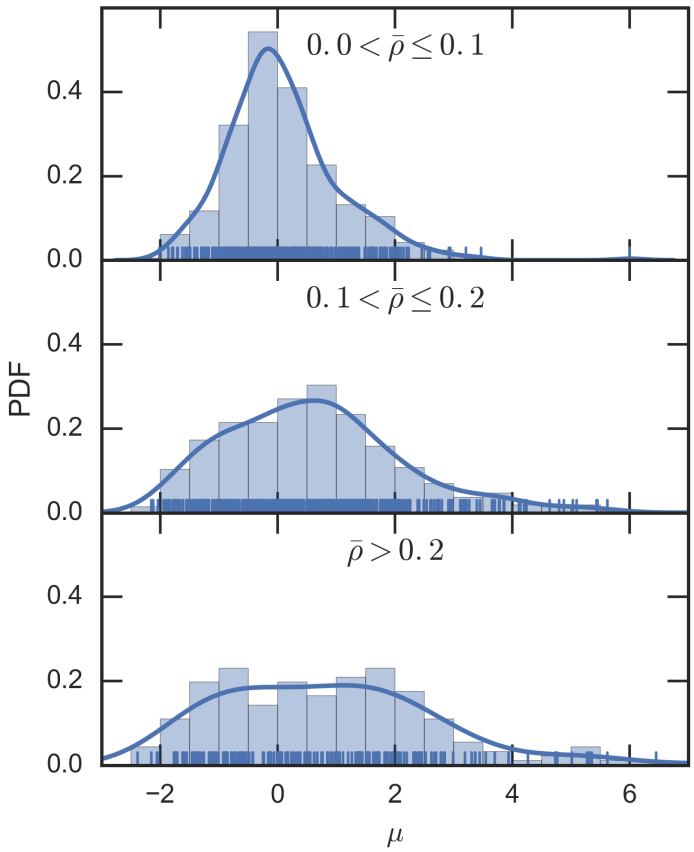

Figure 15. Normalized frequency (bars) and kernel density (line) of the gamma PSD shape factor μ in three ~~bulk~~ ensemble mean density ranges, ~~$[\rho]$~~ $[\bar{\rho}]$ = g cm~~$^{-3}$~~ $^{-3}$.

Table 1. Liquid water equivalent precipitation accumulation measured with Pluvio^2 200 and 400, change in snow depth and maximum and minimum temperature,maximum and minimum relative humidity, mean and maximum wind speed and mean wind direction of the studied snow events. Events before the horizontal line are recorded during the BAECC campaign.

	LWE (mm)		ΔSD	Temp (°C)		RH (%)		Wind (m s^{-1}, °)		
Event	200	400	(cm)	min	max	min	max	mean	max	mean dir.
2014 Jan 31 21:00 - Feb 01 06:00	7.4	7.3	5.1	-9.8	-8.9	84	91	1.6	2.9	138
2014 Feb 12 04:00 - 11:00	1.0	0.9	1.8	- 1	0	96	98	0.6	2.0	170
2014 Feb 15 21:00 - Feb 16 03:00	2.6	2.6	2.5	-2.1	-1	86	97	1.9	2.7	140
2014 Feb 21 16:00 - Feb 22 05:00	5.5	5.2	3.6	-2.7	0	88	98	2.1	3.4	138
2014 Mar 18 08:00 - 19:00	4.4	4.0	7.3	- 3.8	-1.8	76	96	1.2	2.7	155
2014 Mar 20 16:00 - 23:00	6.1	5.9	4.8	- 4.3	-1.3	89	97	2.0	3.4	146
2014 Nov 06 19:00 - Nov 07 14:30	10.5	–	10.3	-2.4	-1.6	95	97	0.8	1.9	238
2014 Dec 18 14:00 - 19:00	2.6	2.2	3.9	-2.3	-0.8	97	98	1.0	1.8	134
2014 Dec 24 08:30 - 13:00	1.3	1.2	1.2	-9.2	-8.9	90	91	0.7	1.5	204
2014 Dec 30 00:30 - 14:00	6.3	5.3	4.9	-10.4	-0.6	91	98	–	–	–
2015 Jan 3 09:00 - 23:50	7.3	7.3	11.9	- 3.9	0	96	98	2.6	5.2	318
2015 Jan 7 01:00 - 20:10	5.4	4.8	2.2	-6.5	-0.8	92	97	1.3	2.8	181
2015 Jan 8 06:00 - 13:30	2.6	2.7	1.6	- 1.9	0	97	99	1.0	2.2	155
2015 Jan 9 18:00 - Jan 10 06:00	3.1	3.1	4.6	-3.7	-0.2	95	98	1.0	3.0	286
2015 Jan 10 22:00 - Jan 11 09:00	0.7	0.6	0.7	-12.6	-4.4	88	95	1.6	3.4	207
2015 Jan 12 21:00 - Jan 13 08:30	12.8	10.9	9.6	-15.7	-9.0	88	94	1.3	3.1	181
2015 Jan 13 22:00 - Jan 14 07:00	–*	2.2	1.9	-8.0	-0.3	94	98	0.5	1.9	134
2015 Jan 16 01:30 - 07:30	–*	5.8	5.2	-1.3	-0.6	92	98	1.9	3.4	154
2015 Jan 18 16:00 - 21:00	1.9	1.9	2.7	-2.4	-0.3	95	97	1.2	2.6	300
2015 Jan 22 21:00 - Jan 23 04:30	2.1	2.0	2.3	-13.3	-12.5	87	90	–	–	–
2015 Jan 23 15:00 - 23:00	1.4	1.2	1.4	-10.1	-8.8	91	93	0.3	1.0	205
2015 Jan 25 09:00 - 16:00	2.8	2.5	1.9	-2.4	-1.7	96	97	0.7	1.7	170
2015 Jan 31 12:00 - Jan 31 23:15	7.0	6.6	5.7	-1.9	-0.4	92	97	1.2	2.6	175

*Pluvio^2 400 was used as data from Pluvio^2 200 was unavailable

Table 2. The prefactors and exponents of $m = a_m D^{b_m}$ derived for exponential PSD with different values of exponent b_v of velocity relation. The mass given in grams and the volume-equivalent diameter proxy in mm.

Dataset	b_m	$a_m(b_v = 0.217)$	$a_m(\ b_v = 0.244)$	$a_m(b_v = 0.256)$
All cases	1.996	1.036e-4	1.045e-4	1.049e-4
BAECC cases	2.002	1.254e-4	1.264e-4	1.269e-4
Winter 2014-2015 cases	2.031	9.679e-5	9.757e-5	9.792e-5

Table 3. The prefactors and exponents of $m = a_m D^{b_m}$ of literature values for comparison plotted in Fig. 12. A conversion from maximum dimension to volume equivalent diameter is done by assuming axis ratio of 0.6.

Study	b_m	a_m
~~Matrosov 2007~~Matrosov 2007 , $0.12\,\mathrm{mm} < D \leq 2.4\,\mathrm{mm}$	2.0	4.2172×10^{-5}
~~Matrosov 2007~~Matrosov 2007 , $2.4\,\mathrm{mm} < D \leq 24\,\mathrm{mm}$	2.5	3.2430×10^{-5}
~~Heymsfield et al. 2004~~ Heymsfield et al. 2004	2.04	7.5814×10^{-5}
~~Mitchell et al. 1990~~ Mitchell et al. 1990	2.0	3.0926×10^{-5}
~~Locatelli and Hobbs 1974~~ Locatelli and Hobbs 1974	1.9	5.1134×10^{-5}